remote sensing

MDPI

Article

The Capabilities of FY-3D/MERSI-II Sensor to Detect and Quantify Thermal Volcanic Activity: The 2020–2023 Mount Etna Case Study

Simone Aveni [1,2,*], Marco Laiolo [2,3], Adele Campus [2], Francesco Massimetti [2] and Diego Coppola [2,3]

[1] Department of Civil, Constructional and Environmental Engineering (DICEA), Sapienza University of Rome, Via Eudossiana 18, 00184 Rome, Italy
[2] Department of Earth Sciences, University of Turin, Via Valperga Caluso 35, 10125 Turin, Italy; marco.laiolo@unito.it (M.L.); adele.campus@unito.it (A.C.); francesco.massimetti@unito.it (F.M.); diego.coppola@unito.it (D.C.)
[3] NATRISK: Centro Interdipartimentale sui Rischi Naturali in Ambiente Montano e Collinare, Università di Torino, Largo Paolo Braccini, 2, 10095 Grugliasco, Italy
* Correspondence: simonesalvatore.aveni@uniroma1.it

Abstract: Satellite data provide crucial information to better understand volcanic processes and mitigate associated risks. In recent years, exploiting the growing number of spaceborne polar platforms, several automated volcanic monitoring systems have been developed. These, however, rely on good geometrical and meteorological conditions, as well as on the occurrence of thermally detectable activity at the time of acquisition. A multiplatform approach can thus increase the number of volcanological-suitable scenes, minimise the temporal gap between acquisitions, and provide crucial information on the onset, evolution, and conclusion of both transient and long-lasting volcanic episodes. In this work, we assessed the capabilities of the MEdium Resolution Spectral Imager-II (MERSI-II) sensor aboard the Fengyun-3D (FY-3D) platform to detect and quantify heat flux sourced from volcanic activity. Using the Middle Infrared Observation of Volcanic Activity (MIROVA) algorithm, we processed 3117 MERSI-II scenes of Mount Etna acquired between January 2020 and February 2023. We then compared the Volcanic Radiative Power (VRP, in Watt) timeseries against those obtained by MODIS and VIIRS sensors. The remarkable agreement between the timeseries, both in trends and magnitudes, was corroborated by correlation coefficients (ρ) between 0.93 and 0.95 and coefficients of determination (R^2) ranging from 0.79 to 0.84. Integrating the datasets of the three sensors, we examined the effusive eruption of Mount Etna started on 27 November 2022, and estimated a total volume of erupted lava of $8.15 \pm 2.44 \times 10^6$ m^3 with a Mean Output Rate (MOR) of 1.35 ± 0.40 m^3 s^{-1}. The reduced temporal gaps between acquisitions revealed that rapid variations in cloud coverage as well as geometrically unfavourable conditions play a major role in thermal volcano monitoring. Evaluating the capabilities of MERSI-II, we also highlight how a multiplatform approach is essential to enhance the efficiency of satellite-based systems for volcanic surveillance.

Keywords: MERSI-II; FY-3D; Etna; MODIS; VIIRS; MIROVA; Volcanic Radiative Power; thermal remote sensing; volcano monitoring

Citation: Aveni, S.; Laiolo, M.; Campus, A.; Massimetti, F.; Coppola, D. The Capabilities of FY-3D/MERSI-II Sensor to Detect and Quantify Thermal Volcanic Activity: The 2020–2023 Mount Etna Case Study. *Remote Sens.* **2023**, *15*, 2528. https://doi.org/10.3390/rs15102528

Academic Editors: Aleksei Sorokin and Olga Girina

Received: 24 March 2023
Revised: 4 May 2023
Accepted: 9 May 2023
Published: 11 May 2023

1. Introduction

Infrared remote sensing of volcanoes has long been a subject of remote sensing studies and has developed into a field of its own since the 1960s [1–3]. Beginning with qualitative observations via aerial and space-born platforms, this discipline has since become a quantitative science, encouraged, and sponsored by leading sensors capable of detecting and monitoring global volcanic activity [2,4]. In the early 2000s, with the advent of its Earth Observing System (EOS) missions, the National Aeronautics and Space Administration (NASA) heralded the beginning of a new era in the field of remote sensing and its

applications [5]. Within this framework, and with regards to volcanological studies, NASA developed The MODerate resolution Imaging Spectroradiometer (MODIS) onboard of Terra (1999) and Aqua (2002) platforms, widely defined as the most successful, volcanologically exploited, and long-lasting sensors produced by NASA [6–10]. The high saturation thresholds of MODIS's thermal bands, coupled with their high temporal resolution, permitted the development of the first automatic global volcanic monitoring system, namely MODVOLC [6,11]. With the revolutionary information and wealth of data provided by MODVOLC, several volcanic hot-spot detection algorithms were developed. Amongst them, the Middle Infrared Observation of Volcanic Activity (MIROVA) developed by [10] is widely described as one the most used algorithm for Near-Real-Time (NRT) quantification of thermal emissions from hot volcanic sources [12–14].

Satellite-derived thermal flux is widely employed to detect signs of unrest in volcanic regions [15–17] and monitor the evolution of volcanic activity [1,12,18]. However, despite a large number of available automatic systems, these are mainly based on individual sensors and/or platforms, resulting either in a limited number of available information, due to temporal constraints or a reduced level of detail, due to the low resolution of the sensors employed (i.e., geostationary platforms) [3]. Additionally, regardless of the amount or the resolution of the available data, all thermal satellite-based systems rely on the availability of scenes acquired in good weather conditions, thus not contaminated by clouds or volcanic plumes, where thermal sources can be clearly distinguished, and thermal energy quantified [8,19]. Furthermore, volcanic processes are typically transient in nature, and variations in the eruptive regime may occur over timescales of tens of minutes [4,20–25]. To track the evolution and detect rapid variations of volcanic activity, researchers employed geostationary satellites, exploiting their high temporal resolution (i.e., from 5 to 15 min for MSG-SEVIRI) [26–29]. Nonetheless, as mentioned above, the low spatial resolution of geostationary platforms (i.e., MSG-SEVIRI, 3 km at nadir) remains a major limitation to precisely locating and quantifying the anomalous thermal source, especially at volcanoes beyond 50°N/S where pixel resolutions exceed 10 km^2 [30]. Moreover, given their relatively static orbital position, geostationary satellites do not provide complete global coverage, resulting in a number of volcanoes (i.e., those sited at the poles) falling outside their Field of View (FOV) [30].

A multiplatform approach based on higher resolution polar satellites can thus reduce the temporal gaps between image acquisitions, increasing the likelihood of acquiring scenes during transient volcanic events, and with good geometrical views, the latter is found to be crucial to correctly identify and quantify the thermal anomalies [12]. Polar imageries acquired with short temporal gaps can also provide crucial information on the evolution of the volcanic activity and its dynamics, for instance, allowing the detection of rapid changes in the eruptive regime, thus in the Time Averaged Discharge Rate (TADR). The rapid response, in turn, allows scientists, stakeholders, and competent bodies to run and update lava flow models, obtaining detailed information on the forthcoming expected scenarios [25].

The majority of global satellite-based volcanological systems have been developed exploiting sensors and polar platforms belonging to the NASA series due to the ease of access and open data policies, length of available timeseries, and indeed, high quality of data provision [10,11,14,31–37]. Nonetheless, although MODIS instruments are still operational, their designated lifetime of 6 years has long overpassed, and although they continue to provide high-quality data, the gradual yet continuous degradation of their capabilities has been widely discussed [38–40]. Ensuring the continuity of satellite-based thermal volcanic systems [14] revealed how the Visible Infrared Imaging Radiometer Suite (VIIRS) sensor aboard Suomi-NPP and NOAA-20 platforms is an excellent candidate to compensate for the forthcoming disposal of Terra and Aqua satellites. Other space agencies, however, have recently launched comparable platforms equipped with sensors able to detect thermal anomalies in volcanic settings, including the European Space Agency (ESA) (i.e., Sentinel-3) [41], the Japan Aerospace Exploration Agency (JAXA) (i.e., GCOM-C) [42]

and the China Meteorological Administration (CMA) (i.e., FY-3D) [25]. Amongst these, the MEdium Resolution Spectral Imager-2 (MERSI-II) aboard Fengyun-3D (FY-3D) platform is of most interest. Several studies assessed and ascertained the similarities between MERSI-II and MODIS [43–49], with [25] suggesting its suitability for volcanological applications. Scholars also revealed that MERSI-II can detect fire hotspot with great accuracy, making it comparable with MODIS fire products [48–53]. However, the evaluation of MERSI-II Medium InfraRed (MIR) bands to detect and quantify thermal volcanic activity is yet to be explored.

In this work, we evaluate, for the first time, the capabilities of the MERSI-II sensor aboard the FY-3D platform to quantify thermal activity, in terms of Volcanic Radiative Power (VRP, Watt) sourced from the volcanic target, by applying the MIROVA algorithm [10]. Taking Mount Etna as a case study, we first provide an overview of the sensor's capabilities, presenting the results obtained from January 2020 to January 2023. We then compare the results obtained by MERSI-II with those obtained by the same algorithm applied to MODIS [10] and VIIRS [14]. Finally, by combining the data retrieved from the three sensors, we provide the Time Averaged Discharge Rate (TADR) and the total erupted volumes for the effusive eruption that commenced the 27 November 2022, highlighting the benefits introduced by operating a multi-platform approach.

2. Mount Etna and Case Study

Mount Etna

Mount Etna is the highest and most active volcano in Europe, sited on the eastern coast of Sicily, Italy [54,55] (Figure 1). The overall volcanic activity alternates between periods of persistent degassing, effusive events, and intense explosive volcanic episodes [56–58]. Beginning with the second decade of the 21st century, the Etnean activity mainly concentrated at its summit craters (Voragine (VOR), Bocca Nuova (BN), North East Crater (NEC), and South East Crater (SEC)) [59]. Within this timeframe, the volcano showed highly explosive phases, characterised by sequences of paroxysms [59–61], alternating with phases of persistent degassing and weak Strombolian activity occasionally associated to poorly fed lava flows from ephemeral sub-terminal vents opened at the base of the summit craters [62]. Paroxysmal episodes are characterised by lava fountains lasting between 1 and 2 h and pyroclastic material ejected up to 3 km above the craters' rims, beyond which conspicuous emissions of volcanic ash are dispersed into the atmosphere for hundreds of kilometers [63]. Lava fountains are often accompanied by short-living lava flows fed by craters' overflows and falling pyroclastic products [63].

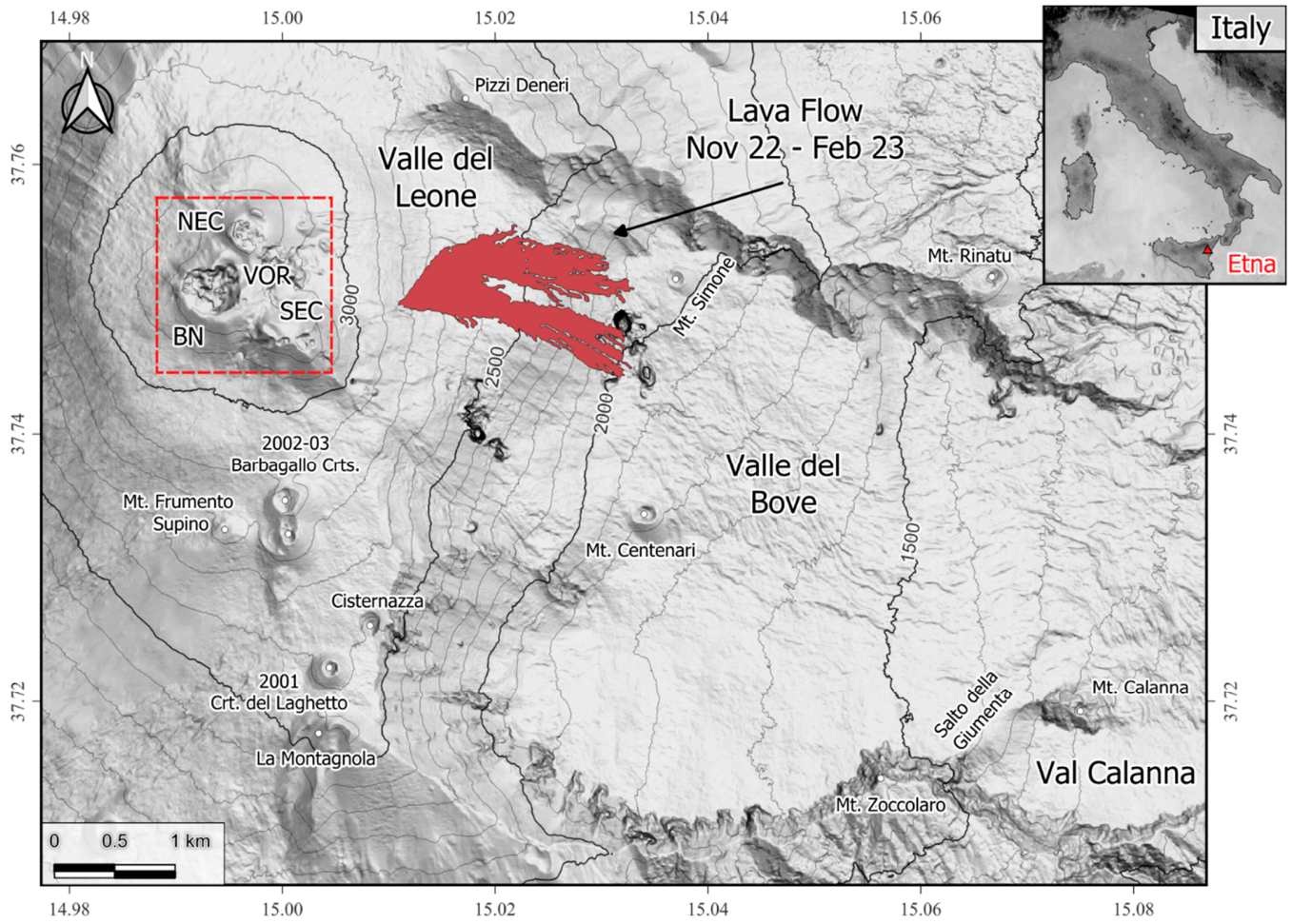

Figure 1. Digital Surface Model (DSM) of Mt. Etna at 2 m spatial resolution derived from 2015 Pleiades Satellite Imagery [64]. The superimposed red shape depicts the extent of the lava flow emplaced during the 27 November 2022–6 February 2023 eruption, as derived from MIROVA-processed [13] Landsat (8–9) and Sentinel-2 (A-B) imageries. The top-right box shows the location map of the study area seen from MERSI-II TIR band (12.0 µm). The red dashed box depicts the summit area and craters, namely Bocca Nuova (BN), North East Crater (NEC), Voragine (VOR), and South East Crater (SEC). The white dots depict the major volcanic structures, as labelled, with Crt(s) standing for Crater(s). Contour lines are derived from the 2 m DSM. Bold black lines show 500 m equidistant intervals, and light black lines are places at 100 m equidistant intervals. The total area of the lava field is comprised of between ~0.88 $\times$ 10^6 and 1.17 $\times$ 10^6 (assuming an error of $\pm$1 pixel).

Between January 2011 and February 2013, the eruptive behavior of Mt. Etna was particularly explosive [65], with 45 paroxysmal episodes recorded within this timeframe (i.e., 76.27% of the total 59 paroxysmal events occurred between 2010–2019) [56]. This intense paroxysmal phase climaxed at the end of 2013 and was replaced by a persistent degassing activity, the latter accompanied by intermittent Strombolian events. On July 2014, the activity underwent drastic changes, with paroxysmal episodes and Strombolian activity being replaced by effusive eruptions originating from the NEC and SEC [65]. The effusive activity lasted until August of the same year [58]. In 2015, after the short effusive eruption of 31 January–2 February (SEC), the activity moved to VOR, producing, between December 2015 and May 2016, the most energetic paroxysmal events at Mount Etna since the beginning of the 21st Century [66–69].

With the termination of paroxysmal episodes at VOR, a new shift in the eruptive style and a decrease in the eruptive frequency was reported by [65]. Between February–April 2017 an effusive event originated from the SEC, later followed by the so-called "Christmas

Eve" flank eruption, which occurred between 24 and 27 December 2018. Overall, between January 2014 and June 2019, 14 paroxysms and 5 main subterminal/flanks eruptions were reported [25,56,70].

The 2020–2023 Volcanic Activity Case Study

Beginning with the third decade of the 2000s, and precisely between April 2020 and February 2022, a new cycle of frequent paroxysms from the SEC crater interrupted the 18-month-long period of low and infrequent activity [24]. Within this biennium, 67 episodes lasting between ~5 and ~800 min having an average duration of ~120 min, and an occurrence rate comprised between 10 to 50 h were reported by [59,71,72]. Paroxysmal episodes alternated with recurrent summital, mostly intracrateric, strombolian activity. The sequence of paroxismal events ceased after February 2022, and, after ~3 months of rest, on 12 May 2022, a new lava flow from the SEC was observed [73]. The effusive activity gradually decreased and terminated between 12–15 June [71,73]. Following this event, the volcano underwent a period of relative quiescence, with sporadic intracrateric explosions and occasional strombolian activity reported from the summit craters.

After a six-month break, the 27 November 2022, a new eruptive fissure opened at the northeastern base of the SEC at ~2800 m a.s.l. [74]. Unfavourable meteorological conditions prevented clear observations of the volcanological phenomenon until 28 November when, as evinced from MIROVA-processed [13] Sentinel and Landsat thermal imageries, disbandment of the cloud cover revealed a second eruptive fissure, sited at ~2900 m a.s.l. in the same sector of the volcano. The mostly effusive activity, at its initial stage, produced a contained lava flow reaching ~2700 m a.s.l. in the Valle del Leone (Figure 1). The activity continued throughout December, with the main lava flow reaching ~2300 m a.s.l. in the Valle del Bove. The eruption maintained a mostly steady trend until the night between 17 January 2022, when a sudden decrease in the effusive regime almost announced the termination of the volcanic event. On January 19th, the effusion reinvigorated, originating two lava flows directed to north-east, skirting the western edge of the cooling lava field and eastward on the steep western flank of Valle del Bove, respectively. As of January 19th, the further extending new fronts were confined at approximately ~2500 m a.s.l. The effusive activity continued throughout January with a relatively low, yet variable, regime until the early hours of February 1st, when a sudden decrease in volcanic activity was observed. On February 2nd, the effusive activity resumed, with new lava flows superimposing the cooling lava field. Between the 4th and 5th of the same month, a progressive decline in the effusive regime led towards the end of the activity, which ultimately ceased the 6 February 2023, with all lava flows confirmed not actively fed [75]. Supervised processing of MIROVA-elaborated [13] visible and thermal Sentinel-2 A/B and Landsat 8/9 imageries revealed that the lava field was confined on the steep western flank of Valle del Bove, covering a total area comprised between ~0.88×10^6 and 1.17×10^6, in large agreement with the preliminary estimate provided by [75].

3. Sensors and Methods

3.1. Fenguyn-3D and MERSI-II Sensor

To achieve the highest standards in modern meteorological services and numerical weather prediction, on 15 November 2017, a new second-generation Chinese polar-orbit satellite was launched [76]. Fengyun-3D (FY-3D) belongs to the FY-3 series of CMA/NSMC (China Meteorological Administration/National Satellite Meteorological Center), and it is mainly used for multi-spectral observations in all weather conditions. The satellite was placed in polar orbit, with a nominal altitude of 836 km and a repeat cycle of 5.5 days [77,78]. Amongst the 10 sensors equipped on the platform, the MEdium Resolution Spectral Imager-II (MERSI-II) provides imageries both in the visible and infrared portion of the spectrum. MERSI-II data are distributed in 25 bands ranging from 0.470 to 12.0 µm, with 1000 m and 250 m nadir spatial resolutions [77]. The swath of MERSI-II covers an area of 2900 km and operates a whiskbroom 45° scanning mirror to acquire imageries in the across-track

direction, from −55.04° to 55.04° [79]. The scanning mirror is coupled with a 3-reflectors rotating K-mirror to correct the image rotation. The sensor acquires images exploiting two linear multi-detectors perpendicular to the scanning direction: 40 detectors for 250 m resolution bands and 10 detectors for the 1000 m bands [79]. Each file is partitioned and distributed at 5 min intervals in hierarchical data format (HDF5), resulting in a granule size of 2000 (rows) × 2048 (columns) in the 1 km resolution product (1000M_MS). The 1 km resolution file contains the visible (0.470 to 0.865 µm) and the TIR (10.8 and 12.0 µm) bands as aggregated to 1 km from the original 250 m resolution, whilst the remaining 19 channels are provided at the original sampling resolution of 1 km. A separate geolocation file (GEO1K) is also provided, encompassing latitude and longitude information for each pixel, as well as sun and sensor zenith and azimuthal angles, a land/water mask, and a Digital Elevation Model (DEM) [79].

Despite FY-3D being launched with the main purpose of collecting meteorological data, several studies demonstrated how MERSI-II MIR and TIR bands are suitable for detecting and quantifying fire hotspots and anomalous heat sources [50–53]. Indeed, the spectral distribution of MERSI-II channels, as well as its characteristics, make the sensor compared with the bands of MODIS and VIIRS, both in the MIR and TIR regions of the spectrum, i.e., [45,48,49,52,80] (Table 1). In the MIR range—between 3.5 to 4.10 µm—MERSI-II features two InfraRed (IR) channels, namely band 20 and band 21, centred at 3.80 and 4.05 µm, respectively. The two MIR bands of MERSI-II resemble those of MODIS (band 21 and band 22, centred at 3.959 µm) and VIIRS, with a central wavelength of 3.74 (band I-4) and 4.05 (band M-13) µm, in the 375 m and 750 m spatial resolutions, respectively. Similarly, the TIR band of MERSI-II channel 24, centred at 10.8 µm, matches that of band M-15 of VIIRS in the 750 m resolution, while in the 375 m acquisition mode, the VIIRS band I-5 has a slightly higher response, with the central peak placed at 11.45 µm. Finally, MODIS band 31 stands in between, with a central wavelength in the TIR channel of 11.03 µm (Figure 2). These spectral characteristics make MERSI-II perfectly compatible with hotspot detection algorithms typically used in volcanology, including the MIROVA algorithm (see Section 3.3).

Table 1. MERSI-II, MODIS, and VIIRS characteristics. VIIRS bands at 375 m are also included for completeness.

	MERSI-II (FY-3D)	**MODIS (AQUA)**	**VIIRS (NOAA-20)**
Orbit altitude (km)	836	705	824
Equator Crossing time	13:45 LT	13:30 LT	14:20 LT
Swath (km)	2900	2330	3060
Pixel resolution at nadir (km)	1	1	0.75/0.375
Pixel resolution at the edge (km)	>6 *	4	1.5/0.75
ID MIR Band (s)	21	21/22	M-13/I-4
Spectral range (µm)	3.973–4.128	3.929–3.989 3.940–4.001	3.973–4.128 3.550–3.930
TMAX (SNR-NEΔT on orbit)	380 K (0.25)	500 K (0.183) 331 K (0.019)	634 K (0.04)
ID TIR Band (s)	24	31	M-15/I-5
Spectral range (µm)	10.300–11.300	10.780–11.280	10.263–11.263 10.500–12.400
TMAX (SNR-NEΔT on orbit)	330 K (0.4)	400 K (0.017)	343 K (0.03)

* Empirically derived from [78].

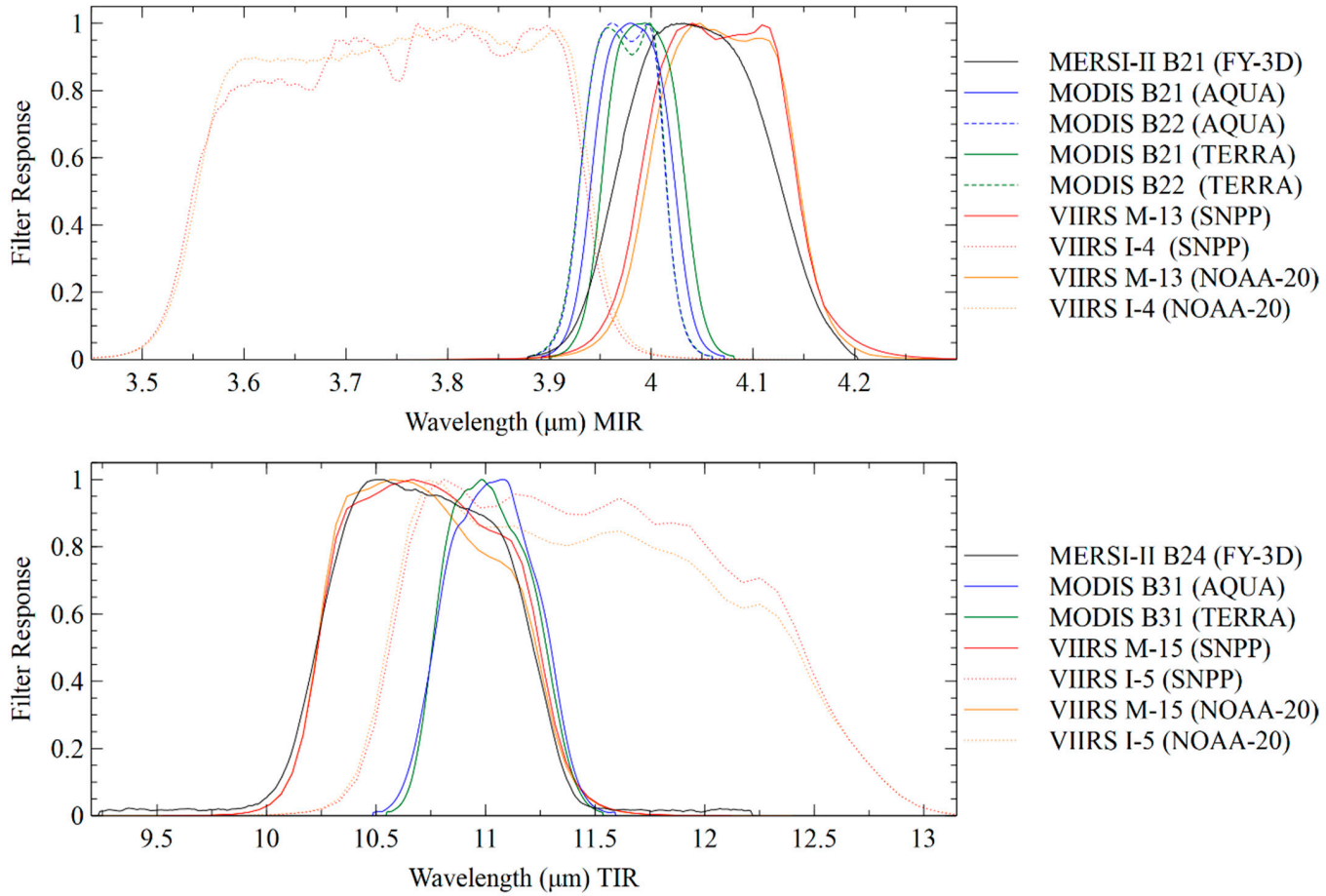

Figure 2. (**Top**) Spectral response functions of MERSI-II, MODIS, and VIIRS in the MIR portion of the spectrum. (**Bottom**) Spectral response functions of MERSI-II, MODIS, and VIIRS in the TIR portion of the spectrum.

3.2. MERSI-II Data Pre-Processing

MERSI-II Level 1 (L1) (FY3D_MERSI_GBAL_L1_yymmdd_hhmm_1000M_MS) and geolocation (FY3D_MERSI_GBAL_L1_yymmdd_hhmm_GEO1K_MS) data are available for download from http://satellite.nsmc.org.cn/PortalSite/Data/Satellite.aspx (accessed on 15 February 2023). From here, we created a spatial subset of the region of interest and downloaded 3117 scenes intersecting Mount Etna, together with the associated geolocation files acquired between January 2020 and February 2023. L1 scientific data are distributed in normalised Digital Numbers (DN). Following [81], DNs were converted to spectral radiance (L) in units of mW/(m^2 cm^{-1} sr) as:

$$L = \text{DN} \times \text{slope} \times \text{intercept} \quad (1)$$

where slope and intercept are available in the file's metadata.

To ensure consistency with MODIS and VIIRS data, as well as compatibility with the spectral range and units used by the MIROVA algorithm, bands 21 and 24 of MERSI-II were selected as MIR and TIR bands, respectively, while radiance values were converted from the original distribution units, namely mW/(m^2 cm^{-1} sr), to W/(m^2 μm sr). A further step was required to ensure imageries were geometrically corrected and pixels affected by the bow-tie phenomenon identified and removed. The bow-tie distortion is, in fact, intrinsically related to the acquisition mode of whiskbroom instruments and relates both to the length of the acquired swath and, in turn, to the earth's curvature and its uneven topography [82]. This results in gradually increasing divergences between regions sensed at the nadir, where the nominal resolution of a given pixel (for MERSI-II 1 km^2) almost

matches the area sensed by the detector, with the edges of the swath, where the area seen by the detectors (for MERSI-II ~6 km—[78]) is projected into a 1 km^2 pixel. As a result, this may introduce scan overlaps between adjacent pixels, with the area sensed by a detector also viewed by adjacent detectors [83]. As discussed by [9], identification and removal of pixels affected by the bow-tie phenomenon is a crucial step in thermal remote sensing of volcanic areas, as duplicate pixels might lead to overestimation of the thermal anomalies, in turn resulting in an erroneous quantification of the associated emitted thermal energy. Consistently with the MIROVA algorithm, we employed the approach proposed by [82] to identify and isolate the pixels affected by bow-tie distortions, ensuring that original granules were free from geometrical artefacts. After applying radiometric and geometric corrections, random scenes were visually inspected to ensure corrections were successful. The inspection revealed a persistent geolocation offset of ~1 pixel westward, both in the ascending and descending acquisition geometries. Indeed, the geolocation inaccuracy of the MERSI-II sensor is not a novelty, and previous studies attempted to quantify and correct the offset [78,79]. Nonetheless, the correction techniques proposed in previous works require computational-elaborate and time-consuming approaches that would compromise the purpose of a potential NRT elaboration. Instead, a 1-pixel shift was hardcoded for all of the scenes, achieving a good trade-off between geolocation accuracy and computational time while ensuring an unbiased application of the MIROVA algorithm (see Figure 9).

3.3. MIROVA Algorithm and Volcanic Radiative Power (VRP)

To assess the capabilities of MERSI-II to detect and quantify thermal volcanic activity, we processed the satellite scenes employing the MIROVA algorithm [10]. MIROVA system elaborates on near-real-time images acquired at ~220 volcanoes globally, exploiting both MODIS and VIIRS sensors [14] to detect and quantify thermal volcanic activity. Following the MIROVA structure, MERSI-II bands 21 and 24 were resampled to a regular UTM 51 × 51 km grid, centred on the volcano's summit as per coordinates provided by the Global Volcanism Program [84]. Employing spectral and spatial filters, the first step of the algorithm identifies thermally anomalous pixels within the investigated scene (i.e., hotspots). Using a revised MIR method [85], anomalous pixels are then employed to estimate the magnitude of the radiant power in VRP (see [9,10,85] for a comprehensive review) as:

$$VRP = \Delta L_{MIR} \times \frac{\sigma \varepsilon}{\alpha \varepsilon_{MIR}} \times A_{pix} \quad (2)$$

where σ is the Stefan–Boltzmann constant (5.67 × 10^{-8} J s^{-1} m^{-2} K^{-4}), ε and ε_{MIR} are the surface spectral emissivity at all wavelengths and in the MIR channel, respectively (here assumed to equal 1 for the sake of simplicity; [10]), α is a wavelength-dependent constant (see next paragraph), A_{pix} is the pixel area in km^2. In Equation (2) ΔL_{MIR} represents the excess MIR radiance, which can be mathematically expressed as:

$$\Delta L_{MIR} = L_{MIRhot} - L_{MIRbk} \quad (3)$$

where L_{MIRhot} is the radiance resulting from the pixels identified as hotspot/s, and L_{MIRbk} is the radiance of the background, namely the average radiance of the surrounding, non-alerted pixels. For simplicity, when applied to volcanoes, this approach assumes that the emitter is a gray body, which simplifies Equation (2) assuming $\varepsilon/\varepsilon_{MIR} = 1$.

3.4. Determination of α Coefficient for MERSI-II

The application of Equation (2) for the estimation of the VRP requires a calibration of the α coefficient as a function of the specific wavelength of the used MIR channel [85]. Below we describe how this coefficient has been determined for MERSI-II, and, in a multi-sensor approach perspective, we propose a simple method to calculate the same coefficient for other sensors operating in the MIR region.

The spectral radiance emitted by a blackbody at a wavelength λ (in μm) is given by the Planck function:

$$L(\lambda, T) = \frac{c_1}{\lambda^5\left(\exp\left(\frac{c_2}{\lambda T}\right) - 1\right)} \quad (4)$$

where T is the temperature (in K), and c_1 and c_2 are constants of 1.19×10^8 W/m^2 sr μm^{-4} and 1.44×10^4 μm K, respectively [86]. Ref. [85] advised that in the 4 μm region of the spectrum and for a temperature range between 600 K and 1500 K, Equation (4) can be approximated as:

$$L\left(\lambda_{\sim 4\ \mu m}\right) \approx \alpha T^4 \quad (5)$$

where α is the best-fit coefficient of the fourth power relationship between MIR radiance and temperature [85]. This approximation makes Equation (5) similar to the Stefan–Boltzmann law ($M = \sigma T^4$, where σ is the Stephan–Botzmann constant), making the MIR radiance ($L\left(\lambda_{\sim 4\ \mu m}\right)$) and the emittance M (in W m^{-2}) linearly correlated through a coefficient equal to σ/α. The exact value of α depends on the wavelength and can be calculated by inverting Equation (5) as the ratio between MIR radiance and temperature (averaged over the range of temperatures for which the empirical relationship holds).

The α coefficient has been computed over the spectral range comprised between 3.5 and 4.15 μm, that is, the range where MIR bands are centred (Figure 3). Using this approach, we obtained the sensors' specific α coefficients, namely 2.88×10^{-9} (W m^{-4} sr^{-1} μm^{-1} K^{-4}) both for MERSI and VIIRS bands 21 and M-13, respectively, centred at 4.05 μm; and 2.96×10^{-9} (W m^{-4} sr^{-1} μm^{-1} K^{-4}) for MODIS band 21, centred at 3.959 μm.

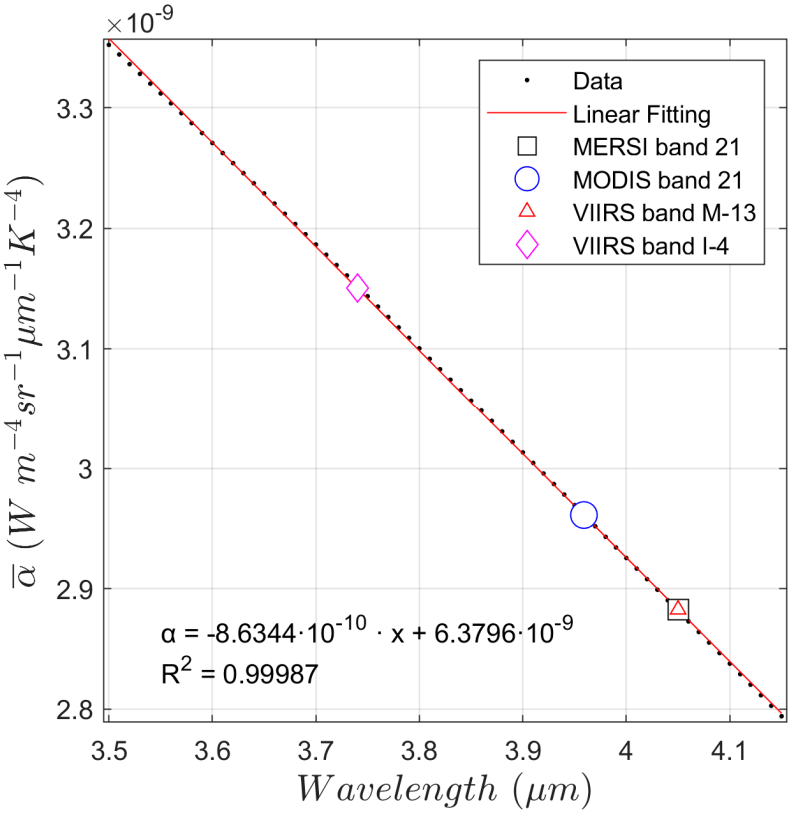

Figure 3. Linear relationship between $\bar{\alpha}$ (W m^{-4} sr^{-1} μm^{-1} K^{-4}) in the range comprised between 600 and 1500 K, and the MIR spectral range, namely 3.5 to 4.15 μm.

Finally, we can rearrange Equation (2) by inclusion of A_{pix} to obtain the sensors' specific VRP calculations.

3.5. Time Averaged Discharge Rates (TADRs) and Total Erupted Volumes

With the specific VRP calculations established, the VRP datasets from each sensor have been combined to obtain the best and most representative thermal signature of the November 2022 effusive event (Section 4.2.2). Following the approach of [87], we visually inspected the elaborated scenes to discard those unsuitable for retrieving the Time Averaged Discharge Rates (TADR), namely those whose detections were clearly attenuated by the presence of clouds and/or by the volcanic plume. We thus calculated the TADR under the assumption that a direct relationship holds between VRP and the TADR [10]:

$$\mathrm{TADR} = \frac{\mathrm{VRP}}{C_{rad}} \tag{6}$$

where C_{rad} (in J m^{-3}) is a case-specific best-fit parameter that expresses the radiant density of the active lava flow encompassing its rheological, insulation, and topographic conditions [88]. Previous works suggested that the C_{rad} of effusive events at Mt. Etna, is comprised between 2.0 and 3.6 $\times$ 10^8 J m^{-3} [10,88]. This range of values embeds the natural variability of the emplacement conditions, which typically characterise Etna lava flows, and has been used to estimate a lower and upper boundary for TADRs (and erupted lava volumes) that characterised the November 2022 eruption.

4. Results

4.1. 2020–2023 MERSI-II Evaluation

A first assessment of MERSI-II capabilities was carried out from January 2020 to February 2023. To ensure an unbiased comparison while maintaining a consistent number of acquisitions between the 3 instruments, we selected one hosting platform for MODIS, and one for VIIRS, namely AQUA and NOAA-20, respectively. The two sensors, in fact, acquire scenes of the investigated region at approximately the same time every day, with gaps spacing from $\pm$5 min to approximately $\pm$1 h, depending on the orbital tracks.

During this time span, all sensors exhibit a quasi-continuous detection of thermally anomalous pixels. The number of acquisitions with at least one alerted pixel was 879, 948, and 1501 over a total of 3117, 2690, and 3105 acquired scenes for MERSI-II, MODIS, and VIIRS, respectively (Table 2). The frequency of detections, computed as the ratio between number of alerted images and the number of overpasses, revealed that MERSI-II distinguished thermal anomalies in 28.20% of the scenes, MODIS in 35.24%, and VIIRS in 48.34%. From the above, it could be suggested that MERSI-II, at least for the investigated region, features a lower sensitivity with respect to NASA's sensors, detecting 19.98% less than MODIS and 41.66% less than VIIRS. Nonetheless, the relative sensitivity of MERSI-II is largely improved when considering only the scenes acquired with zenith angles $\leq 40^\circ$. In fact, on a population of 1262, 1176, and 1223 remaining scenes acquired with zenith angles $\leq 40^\circ$, the fraction of detection was 44.45%, 45.66%, and 57.56%, for MERSI, MODIS, and VIIRS, respectively, resulting in a residual deviation of $-$2.65% when compared to MODIS, and $-$22.78% when compared to VIIRS (Table 2). However, it has to be noted that the larger discrepancies between MERSI-II (and MODIS) and VIIRS sensors can be associated with both the 750 m spatial resolution and the aggregation function developed on VIIRS instruments (see [89]). The aggregation function, in fact, ensures a finer acquisition, increasing the probability of acquiring good scenes and detecting thermal anomalies even at a higher zenith angle. Moreover, the higher VIIRS spatial resolution increases the algorithm sensitivity and, as discussed by [14], directly affects the quantification of the VRP, the latter being strictly related to the spatial distribution of the thermal anomalies.

The VRP timeseries of MERSI show consistent patterns with the other sensors, both in terms of trends and magnitudes (Figure 4). Furthermore, during the analysed period, the three sensors produced consistent VRP values also in terms of average and maximum VRP (Table 2), with the major effusive events reaching maximum values of ~2 GW in all cases. As depicted in Figure 4 and summarised in Table 2, VRP higher than 2 GW and up

to ~20 GW were recorded only during short-lived paroxysmal episodes, in agreement with what was measured by geostationary satellites [90].

Table 2. Comparative summary of MERSI-II, MODIS, and VIIRS datasets used in this study. The number of scenes and the alert frequency (%—in brackets, computed as total number of alerts over the total number of acquisitions) is provided, both for the whole datasets and for scenes acquired with zenith angles $\leq 40°$. Mean and maximum VRPs are also reported.

	MERSI-II (FY-3D)	**MODIS (AQUA)**	**VIIRS (NOAA-20)**
Total scenes	3117	2690	3105
Scenes with alerted pixels	879 (28.20%)	948 (35.24%)	1501 (48.34%)
Scenes with zenith $\leq 40°$	1262	1176	1223
Scenes with alerted pixels (zen. $\leq 40°$)	561 (44.45%)	537 (45.66%)	704 (57.56%)
Mean VRP (MW)	253.69	306.07	192.22
MAX VRP (MW)	18126	18089	21748

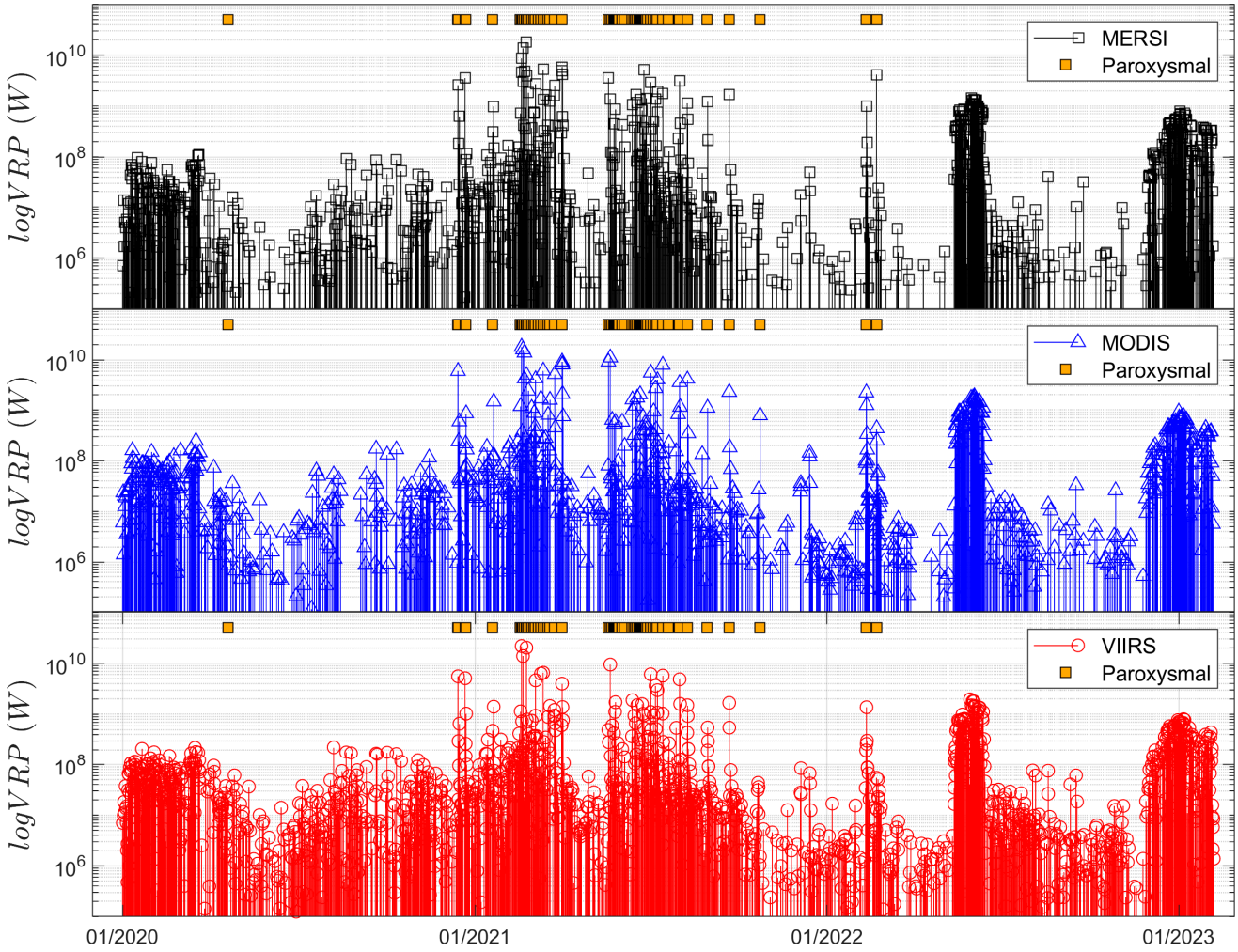

Figure 4. VRP timeseries of Mount Etna between 2020–2023 obtained from the MIROVA algorithm by MERSI-II (**black squares**), MODIS (**blue triangles**), and VIIRS (**red circles**). Orange squares at the top of each panel depict the paroxismal episodes that occurred within the investigated period.

The distribution of the anomalies detected by the three sensors was further investigated to evaluate potential incongruencies arising from the different saturation thresholds, sensitivities, and spectral characteristics (Table 1). Figure 5a,b outline how the alert's

magnitude of all sensors exhibits consistent, slightly right-skewed distributions, with modal values comprised between 10 and 50 MW (log10 VRP = 7–7.5 in Figure 5a,b), in agreement with the findings of [14] for MODIS and VIIRS. These results are consistent with the ordinary (summit explosive/strombolian) thermal regime of Mount Etna, where values > 100 MW represent lava overflows, effusive eruptions, and paroxysmal/lava fountaining episodes [70,87,91]. Similarly, both minimum and maximum values show equal frequency distributions in spite of the lower saturation limit of MERSI-II. The latter suggests that at least for the activity that occurred at Etna volcano in the 3 analysed years (2020–2023), the lower saturation threshold of MERSI-II did not compromise its capabilities of quantify thermal emissions, this remaining consistent both with MODIS and VIIRS sensors.

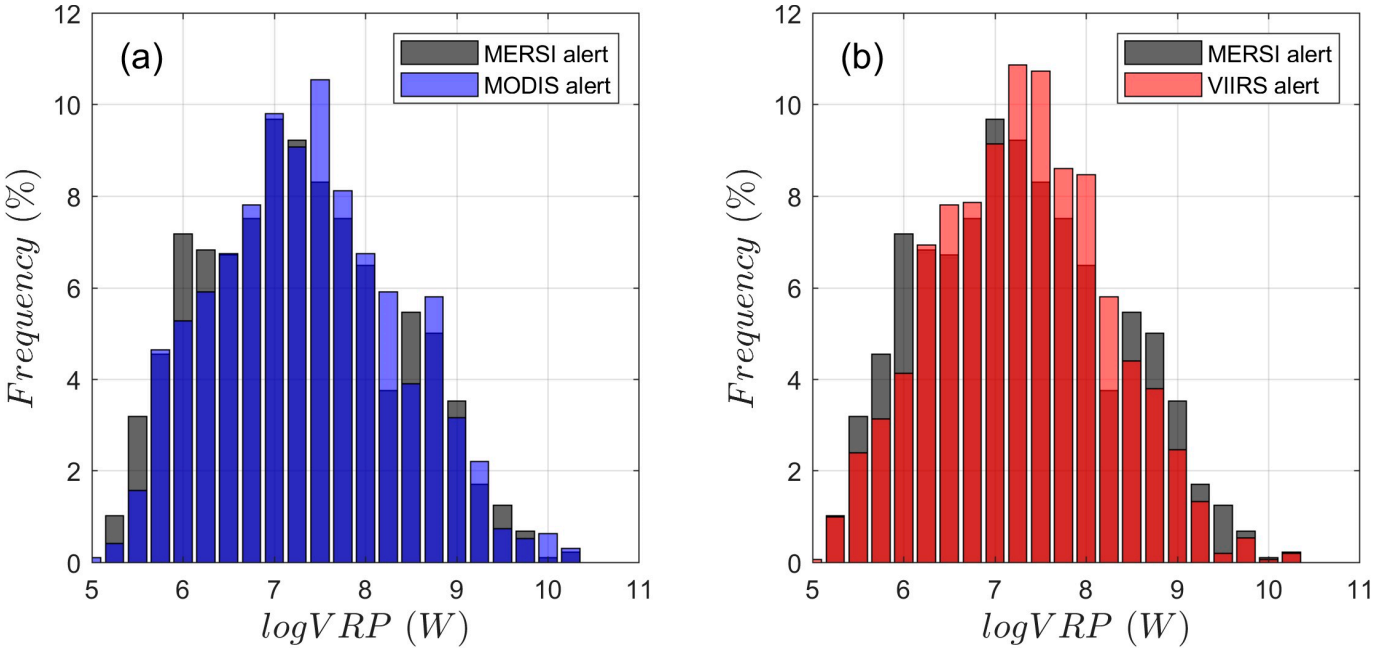

Figure 5. Histograms of VRP magnitudes distribution, expressed as frequency (%) (bin classes 0.25) for the log transformed VRP timeseries for (**a**) MERSI-II and MODIS and (**b**) MERSI-II and VIIRS. The logarithmic scale span from 0.1 MW to 100 GW.

To evaluate the correlation between the three datasets, we homogenised the time series by computing the weekly mean of VRP ($\overline{VRP}$) (Figure 6a). We thus produced the related coefficient of determination plots for the whole datasets (Figure 6b–d).

This analysis corroborates the similarities previously observed in Figures 4 and 5, with all of three sensors showing consistent trends and patterns. To ensure statistical accuracy, we first tested the dataset distributions for normality by mean of the Shapiro-Wilk test. The latter confirmed the non-normal distribution of the timeseries, leading us to employ non-parametric measures of correlation. As such, the visual similarities between timeseries were statistically quantified by mean of the Spearman correlation, returning ρ coefficients comprised between 0.93 and 0.95, and p-values ≤ 0.005, confirming the statistical robustness and very strong association between all the variables. We then retrieved the coefficients of determination (R^2) and the best-fit coefficients (m) for all the $\overline{VRP}$ pairs. The R^2 ranged from 0.79 to 0.84, supporting the solid agreement between the timeseries. In contrast, the best-fit coefficients fluctuated from 0.59 to 1.13. These, however, are particularly sensitive to outliers. As the scenes are acquired with gaps from ~5 min to ~1 h, the presence of outliers further supports the claim that variations in eruptive regimes, cloud coverage, wind, and volcanic plume direction, as well as acquisition geometries, highly influence the remotely sensed thermal information.

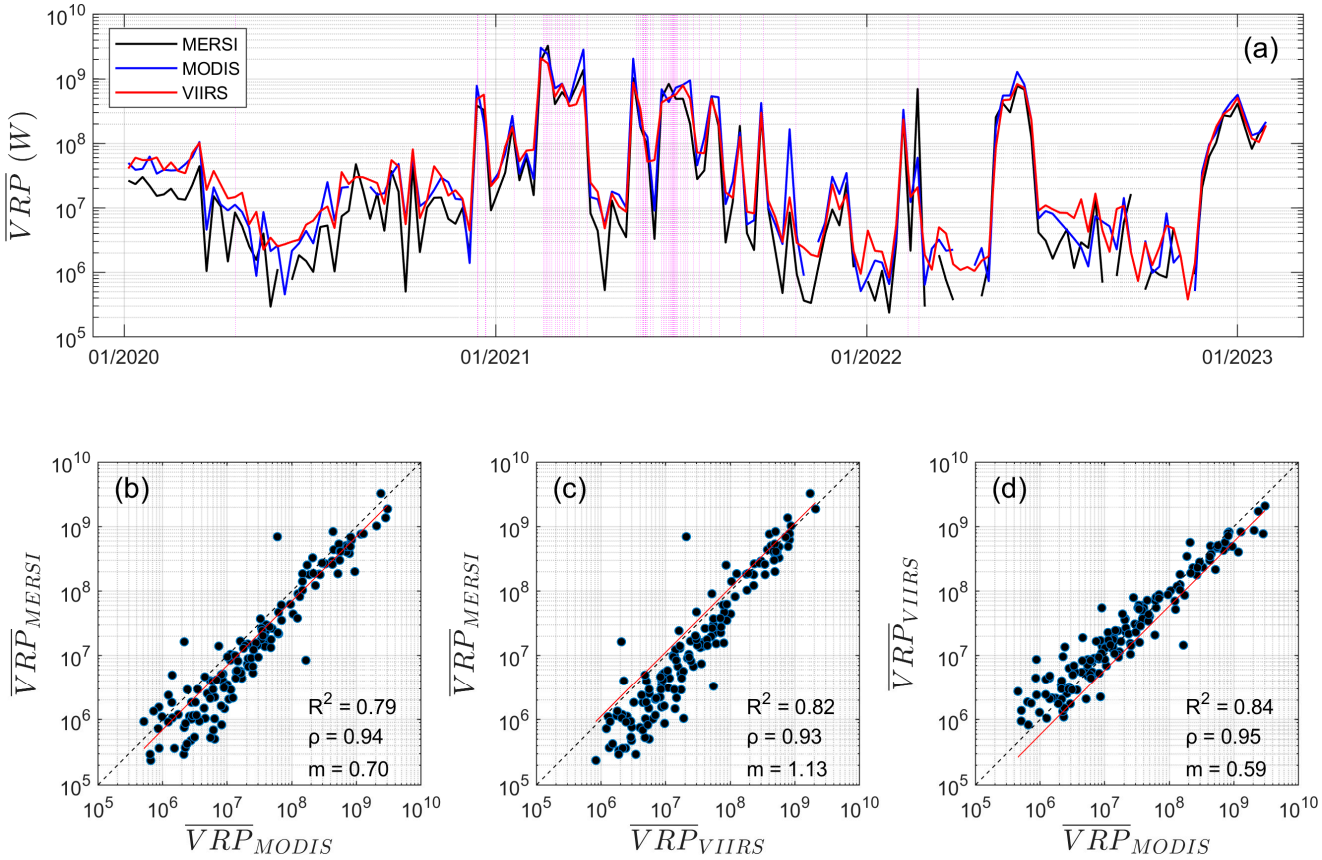

Figure 6. (**a**) Weekly mean VRP timeseries for MERSI-II (in black), MODIS (in blue), and VIIRS (in red). Linear regression plots of weekly mean VRP for (**b**) MERSI-II and MODIS, (**c**) MERSI-II and VIIRS, and (**d**) VIIRS and MODIS. Statistical parameters (Spearman correlation coefficients (ρ), coefficients of determination (R^2), and best-fit coefficients (m)), are also displayed. Note that all plots are presented in logarithmic scale for display purposes.

The effects that suddenly changing conditions have on the correlation between datasets are particularly evident when comparing the Radiated Volcanic Energy (VRE) and their cumulative curves, with the latter proven to be a crucial parameter to investigate the energy associated with volcanic activity [14] and the erupted volumes [88]. The VRE curves were computed by integration of the weekly $\overline{VRP}$ time series during the whole investigated period. In order to avoid, or at least mitigate for decorrelations introduced by transient volcanic activity (i.e., paroxysms), which, in terms of VRP retrieval, is largely affected by temporal constraints (i.e., lags between acquisitions) and meteorological factors (i.e., mutable cloud coverage between acquisitions), the VRE were computed both for the entire (unfiltered) dataset (Figure 7a), and for the datasets filtered for VRP $\leq$ 2 GW (Figure 7b).

The cumulative VRE time series in Figure 7a illustrate the effect of the highly variable conditions of the scene (both eruptive and meteorological) within tens of minutes (i.e., the lag between acquisitions). From a closer inspection, it can be appreciated how the main incongruencies between the time series become evident with the advent of high-energy paroxysmal episodes, which occurred between the 18 and 23 February 2021. This evidence is in line with the findings of previous works (i.e., [4,21–25]), which suggested that variations in explosive and/or eruptive regimes, as well as meteorological conditions, can take place within minutes, drastically affecting satellite-retrieved thermal information. Figure 7b further supports this claim, with the cumulative VRE curves computed after excluding the detections associated with the thermally extreme and transient paroxysmal events (VRP $\geq$ 2 GW). From the above, it emerges how the three sensors show a large agreement, both in terms of trends and magnitudes, when the eruptive regime remained

relatively stable through time. Nonetheless, the incongruencies encountered during the 67 paroxysmal episodes that occurred between April 2020 and February 2022 emphasise the benefits introduced by operating a multiplatform approach for volcanic surveillance. The histogram in Figure 8 corroborates this claim, showing the paroxysmal detection frequency for each sensor individually and for all sensors combined. The detection frequency for each sensor alone spaced between 56.72% and 58.21%, while remarkably increased by more than 10% when all sensors were combined, achieving a total detection rate of 68.66%. This demonstrates how differences in acquisition times, as well as intensity of the volcanic activity, meteorological conditions, and/or location of the volcanic plume at the time of acquisition, dictate the detection capabilities of remotely sensed thermal data, emphasising the contribution that a multiplatform approach can bring into already-operative volcano monitoring systems.

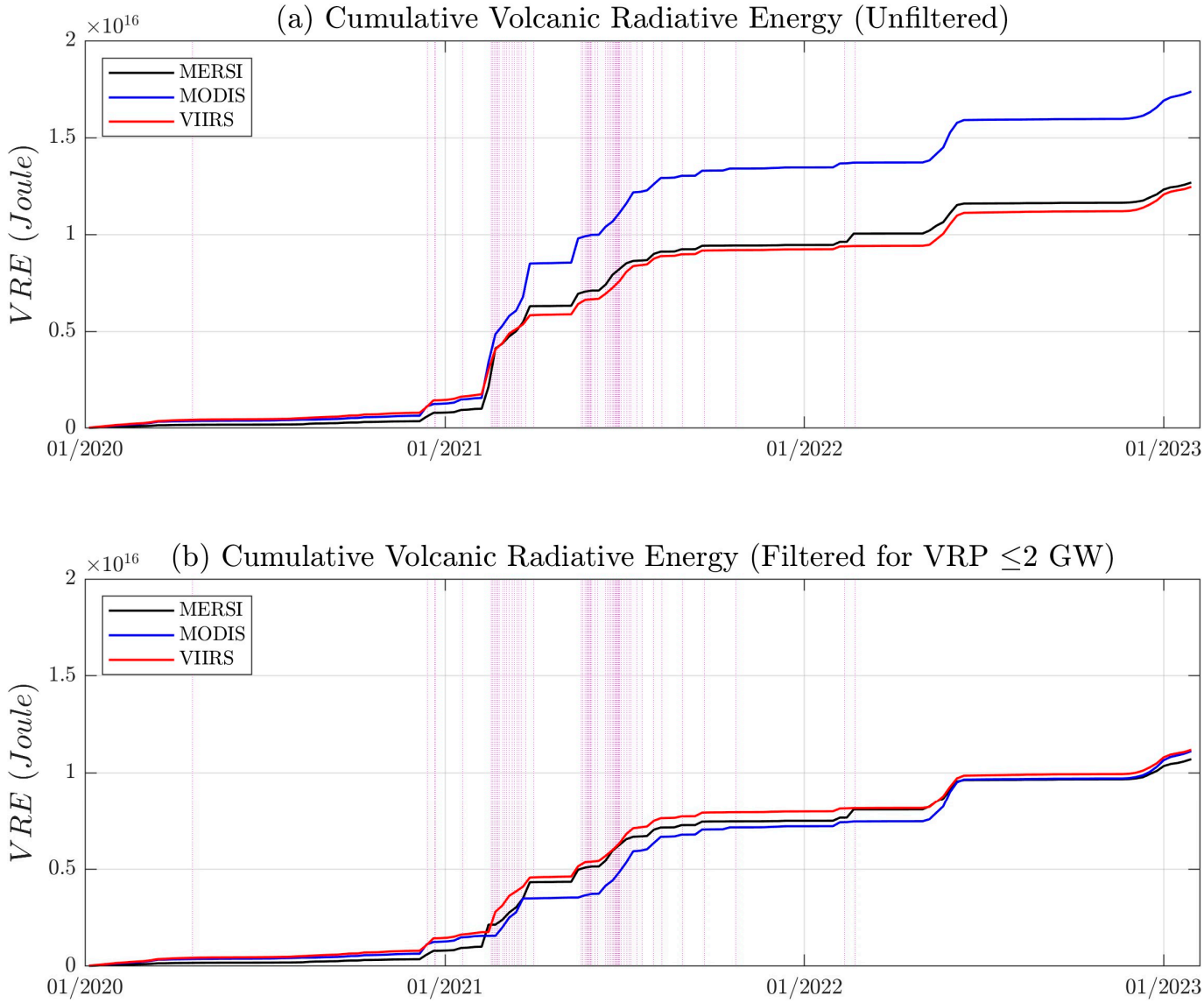

Figure 7. Cumulative curves of Volcanic Radiative Energy computed (**a**) for the whole datasets and (**b**) for the datasets filtered for VRP $\geq$ 2 GW. Note how major discrepancies between cumulative curves arise during transient, thermally extreme, paroxysmal events (magenta dotted vertical lines).

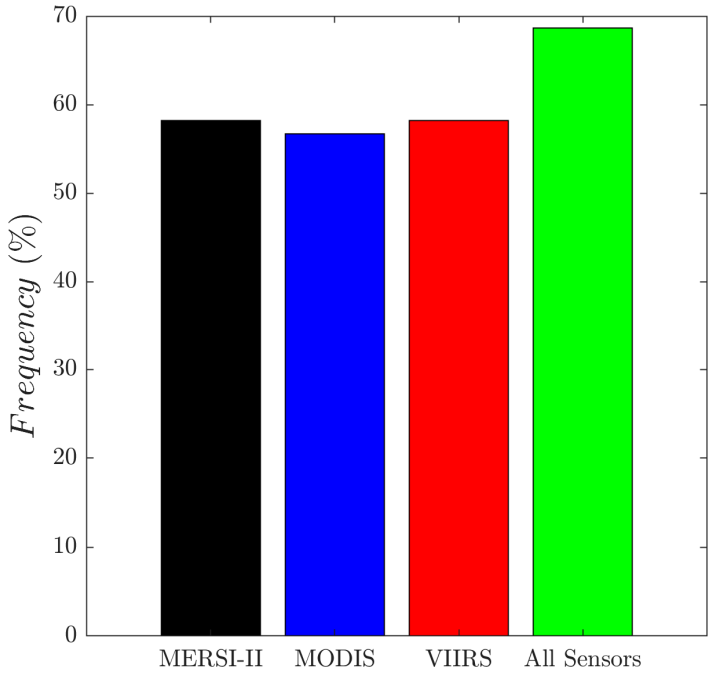

Figure 8. Detection frequency histogram for VRP $\geq$ 100 MW (i.e., above ordinary thermal regime, see text) for MERSI-II (**in black**), MODIS (**in blue**), VIIRS (**in red**), and all sensors combined (**in green**). A margin of $\pm$3 h was added to the start and end time of each paroxismal episode reported by [71]. Note how the total detection frequency increases by more than 10% when all sensors are combined.

4.2. Etna November 2022–February 2023 Eruption

4.2.1. Effect of Viewing Geometry and Cloud Coverage

After assessing the capabilities of MERSI-II to detect and quantify thermal volcanic features and, after positively ascertaining its consistency with the sensors currently in use by the MIROVA system, we combined the three sensors to investigate the effusive eruption of Mount Etna begun on 27 November 2022. First, we investigated the benefits of including an additional sensor in terms of the wealth of data provided, mitigation of cloud-contaminated scenes, and attenuation of detected VRPs related to geometrical constraints. As reported in Table 3, we identified 14 acquisitions between 27 November and 6 February (with a maximum time lag between acquisitions of ~$\pm$1 h) where MERSI-II-retrieved VRPs were higher than those detected both by MODIS and VIIRS. This analysis revealed that in almost half of the scenes where MERSI-II detected higher VRPs than both NASA's sensors, the discrepancies were >100 MW. To better understand the factors leading to these divergences, we visually inspected the TIR scenes having a ΔVRP > 100 MW (Figure 9). TIR scenes were preferred to the respective MIR imageries as clouds are better defined and in turn distinguishable in the long-wave portion of the spectrum. As a drawback, some scenes in Figure 9 might deceptively seem hot-spot free. This, however, relates to (1) the same color bar being applied to all of the scenes for display purposes and (2) to the different spectral characteristics of the MIR and TIR channels and their response to hot surfaces (see [10] for details).

Figure 9 and Table 3 highlight the influence of viewing geometries on remotely sensed thermal information, as well as the effect of meteorological constraints and cloud attenuation on VRP retrieval. With regard to geometrical implications, it can be noted how as in images acquired almost simultaneously, the only increase in the satellite zenith corresponds to a decrease in the VRP. This, as previously discussed by [92], is partially related to the attenuation of the MIR radiance in the function of the satellite zenith angle due to the increased path length affecting the atmospheric transmittance. Moreover, as discussed in Section 3.2, regions sensed with unfavourable viewing geometry (i.e., high satellite zenith) make the radiance of a potential subpixel hotspot to be integrated over

an area gradually increasing toward the end of the swath and/or eventually masked by the topography. Although this is partially corrected during the resampling step (see [9]), residual artefacts can hardly be removed entirely, resulting in the VRP incongruencies displayed in Figure 9 and summarised in Table 3. In terms of cloud coverage, the sequences depicted in Figure 9d–f,m–o provide clear evidence of the limitations of single VRP measurements intrinsically affected by rapid changes in meteorological conditions. This is further exacerbated in regions with steep topographies (i.e., volcanic edifices) where meteorological conditions change from quasi-clear-sky to mostly cloud-covered within minutes. As such, a multiplatform approach can effectively increase the likelihood of acquiring volcanological-suitable imageries, allowing a better VRP estimation and interpretation of the eruptive dynamics.

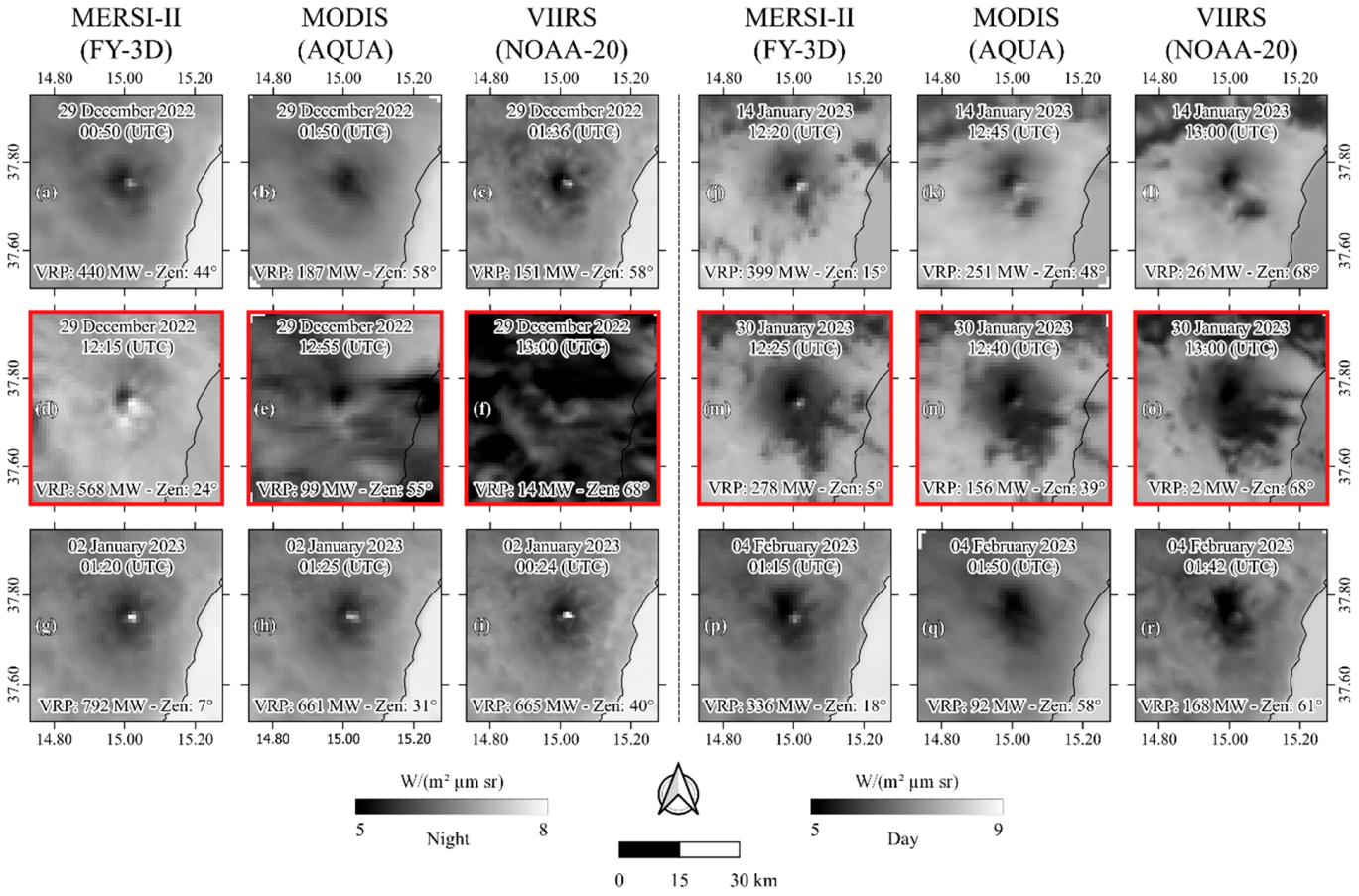

Figure 9. TIR scenes (**a**–**r**) of the acquisitions with VRP discrepancies > 100 MW sensed by MERSI-II (on the **left**), MODIS (in the **middle**), and VIIRS (on the **right**) during the effusive activity of Mount Etna (November 2022–February 2023). Date and time of acquisition is reported at the top of each figure. VRP and zenith angle (°) is also reported at the bottom of each figure. For display purposes, all scenes are represented with the same colormaps, distinguished between day-time and night-time acquisitions, as described at the bottom of the figure. All scenes are centered at Mount Etna summit, with black continuous lines demarking the coastline of Sicily. Figures embedded within red frames (**d**–**f**,**m**–**o**) highlight major VRP discrepancies associated with rapid (~30 min) meteorological variations over the eruptive scene. Note how all MERSI-II scenes are in excellent agreement with the coastline boundaries, revealing how the 1-pixel shift was sufficient to mitigate the geolocation offset (see Section 3.2); also note that some TIR scenes deceptively seem hot-spot free, however, is related to graphical and spectral properties of the scenes (see Section 4.2.1).

Table 3. Temporal and geometrical characteristics of the scenes acquired by MERSI-II (F), MODIS (M), and VIIRS (V), where MERSI-II detected higher VRP than both MODIS and VIIRS sensors. The dates marked by (*) depict the scenes displayed in Figure 9, namely those having a VRP discrepancy > 100 MW.

Date	Time F	Time M	Time V	MW (Zenith°) F	MW (Zenith°) M	MW (Zenith°) V	Δt F/M	Δt F/V	Δt M/V
22 December 2022	01:20	01:45	00:30	463 (4)	80 (56)	452 (32)	−00:25	+00:50	+01:15
23 December 2022	01:00	00:50	00:12	467 (32)	455 (27)	240 (55)	+00:10	+00:48	+00:38
29 December 2022 *	00:50	01:50	01:36	440 (44)	187 (58)	151 (58)	−01:00	−00:46	+00:14
29 December 2022 *	12:15	12:55	13:00	568 (24)	99 (55)	14 (68)	−00:40	−00:45	−00:05
2 January 2023 *	01:20	01:25	00:24	792 (7)	661 (31)	665 (40)	−00:05	+00:56	+01:01
3 January 2023	01:00	00:30	01:42	704 (35)	669 (55)	377 (61)	+00:30	−00:42	−01:12
8 January 2023	01:10	00:45	01:48	662 (24)	657 (38)	306 (65)	+00:25	−00:38	−01:03
12 January 2023	12:55	13:00	11:54	104 (41)	8 (60)	48 (2)	−00:05	+01:01	+01:06
14 January 2023	01:00	01:45	01:36	83 (37)	34 (53)	54 (58)	−00:45	−00:36	+00:09
14 January 2023 *	12:20	12:45	13:00	399 (15)	251 (48)	26 (68)	−00:25	−00:40	−00:15
28 January 2023	01:40	01:50	00:36	343 (28)	120 (57)	241 (23)	−00:10	+01:04	+01:14
30 January 2023	01:05	01:35	01:36	324 (30)	313 (44)	129 (58)	−00:30	−00:31	−00:01
30 January 2023 *	12:25	12:40	13:00	278 (5)	156 (39)	2 (68)	−00:15	−00:35	−00:20
4 February 2023 *	01:15	01:50	01:42	336 (18)	92 (58)	168 (61)	−00:35	−00:27	+00:08

4.2.2. Discharge Rates and Erupted Volumes

The TADR time series obtained from the joint analysis and supervision of the three datasets (MERSI-II, MODIS, and VIIR) is shown in Figure 10. During the first weeks, the eruption showed a low but steadily increasing effusive trend which climaxed around 31 December, where the peak discharge reached ~3.0 ± 0.90 m^3 s^{-1}. Beginning on 6 January 2023, the effusive regime undertook a decreasing trend, lowering to ~1 ± 0.3 m^3 s^{-1} in mid-January. Notably, from the third week of January until the end of the activity, the effusive pattern changes again, showing at least three sudden oscillations with TADR ranging from ~0.2 ± 0.06 to ~1.4 ± 0.42 m^3 s^{-1} (Figure 10a). These effusive pulses were efficiently detected by all three sensors, which allowed the conclusive phase of the eruption to be reconstructed in greater detail (i.e., obtaining at least one optimal acquisition from one or the other sensors and revealing interim pauses in the effusive activity). Remarkably, although the union of the three datasets, no substantial variations were encountered when excluding MERSI-II from the elaboration of the daily averaged TADR nor from the cumulative erupted volume for the November 2022 eruption (Figure 10b). The total volumes of erupted lava were in fact equal to $8.15 \pm 2.44 \times 10^6$ m^3 with the inclusion of MERSI-II data and $8.31 \pm 2.49 \times 10^6$ m^3 when data from the CMA's sensor were excluded from the calculation. Similarly, the Mean Output Rate (MOR) remained quasi-identical, with a MOR of 1.35 ± 0.40 m^3 s^{-1} obtained with the inclusion of all three sensors and 1.39 ± 0.42 m^3 s^{-1} when computed solely with MODIS and VIIRS data (Figure 10). This evidence further corroborates the consistency of MERSI-II data with those of NASA's sensors, supporting the claim that MERSI-II-equipped FY-3 series of satellites could mitigate the loss of information associated with the imminent disposal of TERRA and AQUA platforms. Additionally, the similarities between the three sensors ensure the collection of consistent information to mitigate for volcanologically unsuitable scenes collected by other sensors, for instance, during adverse meteorological conditions (i.e., clouds or volcanic plumes masking) and/or unfavorauble geometrical views (i.e., Figure 9).

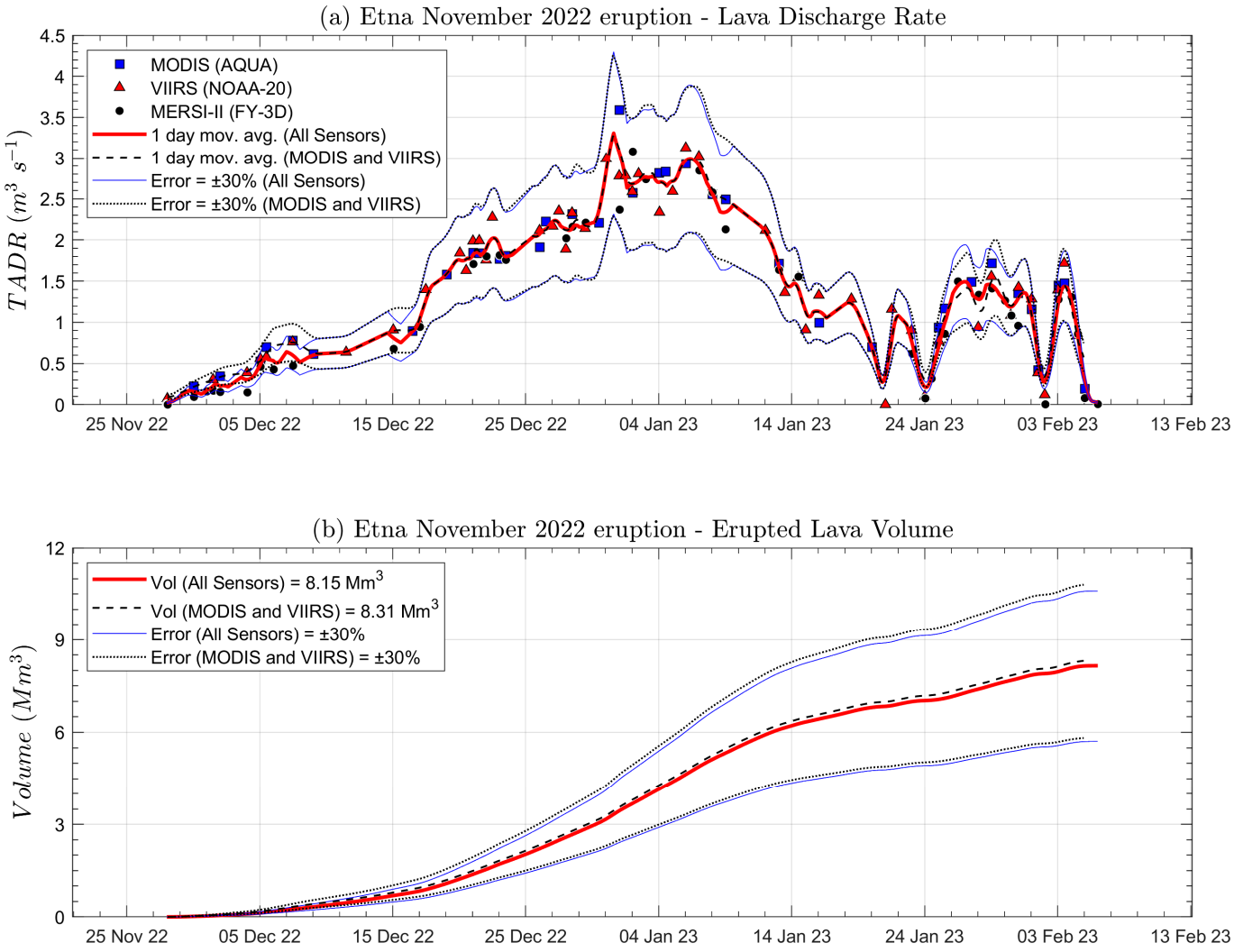

Figure 10. (**a**) Time Averaged Discharge Rates (TADR) computed by integrating the volcanological-suitable scenes from MERSI-II (black dots), MODIS (blue squares), and VIIRS (Red triangles). The red and the black dashed lines represent the 1-day rolling average for the TADR derived by inclusion of all three sensors and for the TADR computed employing only MODIS and VIIRS data, respectively. The solid blue and dotted black lines define the uncertainty boundaries of ± 30% for all sensors and only for MODIS and VIIRS, respectively (as above). (**b**) Cumulative curve of the erupted volume. The red and black dashed lines represent the mean value for all sensors and MODIS and VIIRS, respectively. The blue and the black dotted lines define the uncertainty boundaries of ± 30% for all three sensors and only for MODIS and VIIRS, respectively. The total volumes in Mm^3 are also reported in legend.

5. Discussions and Conclusive Remarks

In this work, for the first time, we assessed the capabilities of MERSI-II MIR bands to detect and quantify thermal volcanic activity and evaluated the benefits of operating a satellite-based multiplatform approach for volcanic surveillance. In particular, we focused on the benefits of introducing additional platforms into already-operating volcanic monitoring systems in order to: (i) provide continuity to VRP timeseries from a multi-decade monitoring perspective and (ii) reduce the temporal gaps between acquisitions by increasing the number of volcanological-suitable scenes (namely those presenting favourable geometrical and meteorological conditions). MERSI-II scenes were acquired for Mount Etna between January 2020 and February 2023 and were processed employing the MIROVA

algorithm. The results were then compared against the data retrieved by MODIS and VIIRS sensors and processed using the same method.

5.1. MERSI Sensors: Limits and Sensitivity

At first, we noted how the lower saturation threshold of MERSI-II positively handled thermally extreme events at Mount Etna, at least up to ~18 GW, revealing almost no differences with MODIS nor VIIRS instruments, in spite of their higher saturation capabilities. Yet, the reduced spatial and temporal extent of the investigation did not allow us to determine whether more energetic volcanic events might result in an underestimation of the emitted thermal energy, and further studies should assess the saturation limits of the sensor. In terms of magnitude consistency, the Volcanic Radiative Power (VRP) timeseries showed excellent agreement, although the weekly $\overline{VRP}$ timeseries in Figure 6a revealed a systematic prevalence of MERSI-II detections in the lower thermal regime (<10 MW). Despite this can be neglected for volcanological applications and did not affect the results obtained in this work, some considerations may suggest that the divergences encountered in the low thermal regime may be related to a higher accuracy of MERSI-II 1000 m TIR bands in quantifying minor thermal anomalies, being this aggregated from the corresponding, higher resolution, 250 m channel [49]. Nonetheless, this investigation goes beyond the purpose of this work, and we envisage future studies will further investigate the above. Corroborating the excellent agreement between the timeseries, we observed correlation coefficients (ρ) comprised between 0.93 and 0.95 and coefficients of determination (R^2) ranging from 0.79 to 0.84. In contrast, the best-fit coefficients oscillated between 0.59 and 1.13, but these values are largely affected by the presence of outliers. Outliers were introduced by significant thermal variations between scenes acquired within ~1 h, implying a drastic variation of the sensed area, either in terms of eruptive regime or cloud/plume coverage. Taking into consideration the reduced temporal gap between acquisitions and considering the ephemeral nature of paroxysmal episodes, we suggest that major thermal inconsistencies observed during 2021–2022 could be, at least partially, related to rapid variations of thermal flux between acquisitions, in line with the findings of previous authors [4,20–25,93]. Nonetheless, this suggestion remains speculative in nature, and further studies are required to ascertain its veracity.

5.2. Advantages of a Multiplatform Approach

With regards to the contribution that a polar multi-platform approach provides in terms of data availability and reliability, we positively fulfilled the aim of this work, validating MERSI-II as a useful sensor for volcanic thermal monitoring in excellent continuity with MODIS and VIIRS. We also present clear and robust evidence of the advantages introduced by reducing the temporal gaps between acquisitions while maintaining a relatively high spatial resolution. During transient eruptive episodes, such as paroxysmal events, for instance, a constellation of volcanological-suitable sensors may draw the line between detection or loss of thermal anomalies. Despite this may be compensated by ground instruments at volcanoes boasting comprehensive and multiparametric monitoring networks, the same may not apply for remote, poorly monitored volcanoes, where remotely sensed data are the only surveillance source. Nonetheless, even at well-monitored volcanoes such as Mount Etna, integration of data retrieved from multiple platforms was crucial to reduce gaps between acquisitions, maximise the number of TADR-suitable scenes, and obtain a more detailed understanding of the ongoing activity. Compared to using a single sensor, the multi-sensor approach has increased the ability to detect paroxysmal events from 56.72% to 68.66%. Similarly, and with regards to the activity of November 2022, a denser dataset enabled us to distinguish sudden variations in the effusive regime that occurred in less than 24 h, otherwise missed, or at least underestimated, without the contribution of the data provided by the additional sensor (see Figure 10). Merging the information obtained by MERSI-II into the MIROVA database, we increased the number of volcanological-suitable scenes by ~31%, obtaining an average of ~2 suitable imageries per day. The higher number of

scenes acquired during the effusive eruption enabled us to determine both the total erupted volume and the Mean Output Rate, namely $8.15 \pm 2.44 \times 10^6$ m^3 and 1.35 ± 0.40 m^3 s^{-1}, respectively.

6. Conclusions

The promising findings of this work provide reliable alternatives to mitigate the imminent disposal of AQUA and TERRA whilst permitting to increase in the amount of information available during their operativity. Notably, in February 2023, the CMA, jointly with the China Aerospace Science and Technology Corporation (CASC), announced the launch of two additional FY-3 series satellites, namely FY-3F and FY-3G, in August and April 2023, respectively [94]. This, coupled with the great effort made by the CMA to constantly improve its Fengyun-3 series of second-generation polar-orbiting satellites, is particularly encouraging and has the potential to provide an unprecedented wealth of data to the volcanological community. In this regard, it is worth mentioning that CMA has already placed into a dawn-dusk orbit the first crepuscular satellite of its kind, namely FY-3E. The latter is equipped with the MERSI-LL (Low-Light) instrument and features both MIR and TIR channels at 1 km resolution. FY-3E senses the globe in the early mornings and afternoons (Equator Crossing Time (ECT) 05:30 am L.T.), with the potential of largely reducing the gaps currently left by sun-synchronous platforms [95]. In fact, the particular acquisition time of this satellite makes it particularly interesting as it can cover a time window otherwise discovered by the other sensors. Although no information is yet available on its suitability for volcanological applications, current studies are being conducted to assess its capabilities and explore the benefits introduced by its usage.

With regards to the current application of MERSI-II data, these can be downloaded on-demand for global targets, increasing the number of scenes and the amount of information available during a volcanic crisis or exploited for more comprehensive a posteriori analysis. At the time of writing, integration of CMA's FY-3 sensors into already-operative automated Near Real Time volcanic monitoring systems remains impossible. In fact, no direct access to the NRT file transfer protocol (FTP) nor unlimited access to the online database is currently available. In this perspective, however, the findings of this manuscript outline the contribution that FY-3 satellites could potentially bring to the volcanological community [96], and we envisage that this work will encourage an unrestricted sharing of data from existing and forthcoming FY-3 missions, allowing scientists, scholars, and observatories to better understand volcanic processes and monitor their behaviour, reducing the risks posed by volcanoes worldwide.

Author Contributions: S.A. and D.C. conceived the paper and developed the algorithm; S.A. wrote the manuscript and prepared figures and tables; all authors contributed to the data processing and analysis; D.C. and M.L. supervised the preparation of the manuscript; D.C., M.L., A.C. and F.M. reviewed the paper. All authors have read and agreed to the published version of the manuscript.

Funding: This research received no external funding.

Data Availability Statement: FY-3D satellite data can be downloaded from the website of the China National Satellite Meteorological Center (http://satellite.nsmc.org.cn/portalsite/default.aspx) (accessed on 15 February 2023). MODIS and VIIRS data can be downloaded from https://lance.modaps.eosdis.nasa.gov/ (accessed on 15 February 2023). The data presented in this work are available on request from the corresponding author.

Acknowledgments: We would like to thank the three anonymous reviewers for their valuable comments which helped improve the quality of the manuscript, and the Editors for their kind availability. MIROVA is a collaborative project between the Universities of Turin and Florence (Italy). We acknowledge the LANCE–MODIS data system for providing MODIS and VIIRS Near Real Time products. We acknowledge ESA and NASA/USGS for providing Sentinel-2 and Landsat imageries via the EO Browser portal (https://apps.sentinel-hub.com/eo-browser/) (accessed on 15 February 2023). This work was supported by the 'Piano Nazionale di Ripresa e Resilienza' (PNRR).

Conflicts of Interest: The authors declare no conflict of interest.

References

1. Ramsey, M.; Harris, A.J.L. How will thermal remote sensing of volcanic surface activity evolve over the next decade? *J. Volcanol. Geotherm. Res.* **2013**, *249*, 217–233. [CrossRef]
2. Harris, A. *Thermal Remote Sensing of Active Volcanoes: A User's Manual*; Cambridge University Press: Cambridge, UK, 2013. [CrossRef]
3. Blackett, M. An Overview of Infrared Remote Sensing of Volcanic Activity. *J. Imaging* **2017**, *3*, 13. [CrossRef]
4. Blackett, M. Early Analysis of Landsat-8 Thermal Infrared Sensor Imagery of Volcanic Activity. *Remote Sens.* **2014**, *6*, 2282–2295. [CrossRef]
5. Ramsey, M.S.; Flynn, L.P. Strategies, insights, and the recent advances in volcanic monitoring and mapping with data from NASA's Earth Observing System. *J. Volcanol. Geotherm. Res.* **2004**, *135*, 1–11. [CrossRef]
6. Wright, R.; Flynn, L.P.; Garbeil, H.; Harris, A.J.L.; Pilger, E. Automated volcanic eruption detection using MODIS. *Remote Sens. Environ.* **2002**, *82*, 135–155. [CrossRef]
7. Watson, I.M.; Realmuto, V.J.; Rose, W.I.; Prata, A.J.; Bluth, G.J.S.; Gu, Y.; Bader, C.E.; Yu, T. Thermal Infrared Remote Sensing of Volcanic Emissions Using the Moderate Resolution Imaging Spectroradiometer. *J. Volcanol. Geotherm. Res.* **2004**, *135*, 75–89. [CrossRef]
8. Rothery, D.A.; Coppola, D.; Saunders, C. Analysis of volcanic activity patterns using MODIS thermal alerts. *Bull. Volcanol.* **2005**, *67*, 539–556. [CrossRef]
9. Coppola, D.D.; Piscopo, M.; Laiolo, C.; Cigolini, D. Delle Donne, and M. Ripepe. Radiative Heat Power at Stromboli Volcano During 2000–2011: Twelve Years of MODIS Observations. *J. Volcanol. Geotherm. Res.* **2012**, *215*, 48–60. [CrossRef]
10. Coppola, D.M.; Laiolo, C.; Cigolini, D.; Delle, D.; Ripepe, M. Enhanced Volcanic Hot-Spot Detection Using MODIS IR Data: Results from the MIROVA System. *Geol. Soc. Lond. Spec. Publ.* **2016**, *426*, 181–205. [CrossRef]
11. Wright, R.; Flynn, L.P.; Garbeil, H.; Harris, A.J.L.; Pilger, E. MODVOLC: Near-real-time thermal monitoring of global volcanism. *J. Volc. Geotherm. Res.* **2004**, *135*, 29–49. [CrossRef]
12. Coppola, D.; Laiolo, M.; Cigolini, C.; Massimetti, F.; Delle Donne, D.; Ripepe, M.; Arias, H.; Barsotti, S.; Parra, C.B.; Centeno, R.G.; et al. Thermal Remote Sensing for Global Volcano Monitoring: Experiences from the MIROVA System. *Front. Earth Sci.* **2020**, *7*, 362. [CrossRef]
13. Massimetti, F.; Coppola, D.; Laiolo, M.; Valade, S.; Cigolini, C.; Ripepe, M. Volcanic Hot-Spot Detection Using SENTINEL-2: A Comparison with MODIS–MIROVA Thermal Data Series. *Remote Sens.* **2020**, *12*, 820. [CrossRef]
14. Campus, A.; Laiolo, M.; Massimetti, F.; Coppola, D. The Transition from MODIS to VIIRS for Global Volcano Thermal Monitoring. *Sensors* **2022**, *22*, 1713. [CrossRef] [PubMed]
15. Furtney, M.A.; Pritchard, M.E.; Biggs, J.; Carn, S.A.; Ebmeier, S.K.; Jay, J.A.; McCormick Kilbride, B.T.; Reath, K.A. Synthesizing multi-sensor, multi-satellite, multi-decadal datasets for global volcano monitoring. *J. Volcanol. Geotherm. Res.* **2018**, *365*, 38–56. [CrossRef]
16. Reath, K.; Pritchard, M.; Poland, M.; Delgado, F.; Carn, S.; Coppola, D.; Andrews, B.; Ebmeier, S.K.; Rumpf, E.; Henderson, S.; et al. Thermal, deformation, and Degassing remote Sensing time Series (CE 2000–2017) at the 47 most active volcanoes in Latin AMERICA: Implications for volcanic systems. *J. Geophys. Res. Solid Earth* **2019**, *124*, 195–218. [CrossRef]
17. Girona, T.; Realmuto, V.; Lundgren, P. Large-scale thermal unrest of volcanoes for years prior to eruption. *Nat. Geosci.* **2021**, *14*, 238–241. [CrossRef]
18. Laiolo, M.; Massimetti, F.; Cigolini, C.; Ripepe, M.; Coppola, D. Long-term eruptive trends from space-based thermal and SO2 emissions: A comparative analysis of Stromboli, Batu Tara and Tinakula volcanoes. *Bull. Volcanol.* **2018**, *80*, 68. [CrossRef]
19. Murphy, S.W.R.; Wright, C.; Oppenheimer, C.; Souza Filho, R. MODIS and ASTER Synergy for Characterizing Thermal Volcanic Activity. *Remote Sens. Environ.* **2013**, *131*, 195–205. [CrossRef]
20. Ramsey, M.S.; Harris, A.J.L.; Watson, I.M. Volcanology 2030: Will an orbital volcano observatory finally become a reality? *Bull. Volcanol.* **2022**, *84*, 6. [CrossRef]
21. Harris, A.J.L.; Murray, J.B.; Aries, S.E.; Davies, M.A.; Flynn, L.P.; Wooster, M.J.; Wright, R.; Rothery, D.A. Effusion rate trends at Etna and Krafla and their implications for eruptive mechanisms. *J. Volcanol. Geotherm. Res.* **2000**, *102*, 237–270. [CrossRef]
22. NC, L.; AJL, H.; JE, B.; Ripepe, M.; Calvari, S.; Dehn, J.; Rowland, S. Pulsed lava effusion at Mount Etna during 2001. *J. Volcanol. Geotherm. Res.* **2004**, *137*, 231–246.
23. Bailey, J.E.; Harris, A.J.L.; Dehn, J.; Calvari, S.; Rowland, S.K. The changing morphology of an open lava channel on Mt. Etna. *Bull. Volcanol.* **2006**, *68*, 497–515. [CrossRef]
24. Calvari, S.; Bonaccorso, A.; Ganci, G. Anatomy of a Paroxysmal Lava Fountain at Etna Volcano: The Case of the 12 March 2021, Episode. *Remote Sens.* **2021**, *13*, 3052. [CrossRef]
25. Aveni, S.; Blackett, M. The first evaluation of the FY-3D/MERSI-2 sensor's thermal infrared capabilities for deriving land surface temperature in volcanic regions: A case study of Mount Etna. *Int. J. Remote Sens.* **2022**, *43*, 2777–2792. [CrossRef]
26. Gouhier, M.; Harris, A.; Calvari, S.; Labazuy, P.; Guéhenneux, Y.; Donnadieu, F.; Valade, S. Lava discharge during Etna's January 2011 fire fountain tracked using MSG-SEVIRI. *Bull. Volcanol.* **2012**, *74*, 787–793. [CrossRef]
27. Corradini, S.; Guerrieri, L.; Lombardo, V.; Merucci, L.; Musacchio, M.; Prestifilippo, M.; Scollo, S.; Silvestri, M.; Spata, G.; Stelitano, D. Proximal Monitoring of the 2011–2015 Etna Lava Fountains Using MSG-SEVIRI Data. *Geosciences* **2018**, *8*, 140. [CrossRef]

28. Corradini, S.; Guerrieri, L.; Stelitano, D.; Salerno, G.; Scollo, S.; Merucci, L.; Prestifilippo, M.; Musacchio, M.; Silvestri, M.; Lombardo, V.; et al. Near Real-Time Monitoring of the Christmas 2018 Etna Eruption Using SEVIRI and Products Validation. *Remote Sens.* **2020**, *12*, 1336. [CrossRef]
29. Ganci, G.; Harris, A.J.L.; Del Negro, C.; Guehenneux, Y.; Cappello, A.; Labazuy, P.; Calvari, S.; Gouhier, M. A year of lava fountaining at Etna: Volumes from SEVIRI, Geophys. *Res. Lett.* **2012**, *39*, L06305. [CrossRef]
30. Poland, M.P.; Lopez, W.; Pavolonis, M.J. Forecasting, Detecting, and Tracking Volcanic Eruptions from Space. *Remote Sens. Earth Syst. Sci.* **2020**, *3*, 55–94. [CrossRef]
31. Dean, K.G.; Dehn, J.; Engle, K.; Izbekov, P.; Papp, K.; Patrick, M. Operational Satellite Monitoring of Volcanoes at the Alaska Volcano Observatory. In *Monitoring Volcanic Hotspots Using Thermal Remote Sensing, Advances in Environmental Monitoring and Modelling*; Harris, A.J.H., Wooster, M., Rothery, D.A., Eds.; U.S. Geological Survey Advances in Environmental Monitoring and Modelling: Reston, VA, USA, 2002; Volume 1, pp. 70–97.
32. Davies, D.K.; Ilavajhala, S.; Wong, M.M.; Justice, C.O. Fire information for resource management system: Archiving and distributing modis active fire data. *IEEE Trans. Geosci. Remote Sens.* **2009**, *47*, 72–79. [CrossRef]
33. Kaneko, T.; Yasuda, A.; Aoki, Y.; Kajiwara, K.; Kitagawa, S. Realtime monitoring of active volcanoes in East Asia using MODIS and MTSAT data its advancement by GCOM-C1 SGLI. *Int. Arch. Photogramm. Remote Sens. Spatial Inform. Sci.* **2010**, *38*, 209–212.
34. Elvidge, C.D.; Zhizhin, M.; Hsu, F.; Baugh, K.E. VIIRS nightfire: Satellite pyrometry at night. *Remote Sens.* **2013**, *5*, 4423–4449. [CrossRef]
35. Schneider, D.J.; Randall, M.; Parker, T. Volcview: A web-based platform for satellite monitoring of volcanic activity and eruption response. In Proceedings of the Abstract ID IN41D-05 Presented at Fall Meeting 2014, San Francisco, CA, USA, 15–19 December 2014; American Geophysical Union: San Francisco, CA, USA.
36. Pergola, N.; Coviello, I.; Filizzola, C.; Lacava, T.; Marchese, F.; Paciello, R.; Tramutoli, V. A review of RSTVOLC, an original algorithm for automatic detection and near-real-time monitoring of volcanic hotspots from space. *Geol. Soc. Lond. Spec. Publ.* **2016**, *426*, 55. [CrossRef]
37. Gordeev, E.I.; Girina, O.A.; Lupyan, E.A.; Sorokin, A.A.; Kramareva, L.S.; Efremov, V.Y.; Kashnitskii, A.V.; Uvarov, I.A.; Burtsev, M.A.; Romanova, I.M.; et al. The volsatview information system for monitoring the volcanic activity in Kamchatka and on the Kuril Islands. *J. Volcanol. Seismol.* **2016**, *10*, 382–394. [CrossRef]
38. Barnes, W.L.; Xiong, X.; Salomonson, V.V. Status of terra MODIS and aqua modis. *Adv. Space Res.* **2003**, *32*, 2099–2106. [CrossRef]
39. Xiong, X.K.-F.; Chiang, A.; Wu, W.L.; Barnes, B.; Guenther, V.; Salomonson, V. Multiyear On-Orbit Calibration and Performance of Terra MODIS Thermal Emissive Bands. In *IEEE Transactions on Geoscience and Remote Sensing*; IEEE Xplore: Piscataway, NJ, USA, 2008; Volume 46, pp. 1790–1803. [CrossRef]
40. Xiong, X.; Butler, J.J. MODIS and VIIRS Calibration History and Future Outlook. *Remote Sens.* **2020**, *12*, 2523. [CrossRef]
41. Corradino, C.; Ganci, G.; Bilotta, G.; Cappello, A.; Del Negro, C.; Fortuna, L. Infrared Remote Sensing of Volcanic Activity Using Sentinel-3 Images. *Geophys. Res. Abstr.* **2019**, *21*, EGU2019–1226–1221.
42. Kaneko, T.; Yasuda, A.; Takasaki, K.; Nakano, S.; Fujii, T.; Honda, Y.; Kajiwara, K.; Murakami, H. A new infrared volcano monitoring using GCOM-C (SHIKISAI) satellite: Applications to the Asia-Pacific region. *Earth Planets Space* **2020**, *72*, 115. [CrossRef]
43. Yan, L.; Hu, Y.; Li, X.; Li, J.; Zhang, Y.; Dou, C.; Plaza, J.; Plaza, A. Radiometric calibration of Fengyun-3D MERSI-II satellite: A case study in Lake Qinghai, China. In Proceedings of the GARSS 2020—2020 IEEE International Geoscience and Remote Sensing Symposium, Virtual, 26 September–2 October; IEEE: Piscataway, NJ, USA, 2020. [CrossRef]
44. Du, W.; Qin, Z.; Fan, J.; Zhao, C.; Huang, Q.; Cao, K.; Abbasi, B. Land Surface Temperature Retrieval from Fengyun-3D Medium Resolution Spectral Imager II (FY-3D MERSI-II) Data with the Improved Two-Factor Split-Window Algorithm. *Remote Sens.* **2021**, *13*, 5072. [CrossRef]
45. Zeng, H.; Ren, H.; Nie, J.; Zhu, J.; Ye, X.; Jiang, C. Land Surface Temperature and Emissivity Retrieval from Nighttime Middle and Thermal Infrared Images of Chinese Fengyun-3D MERSI-II. *IEEE J. Sel. Top. Appl. Earth Obs. Remote Sens.* **2021**, *14*, 7724–7733. [CrossRef]
46. Dejun, Z.; Shiqi, Y.; Liang, S.; Xiaoran, L.; Shihao, T.; Hao, Z.; Qinyu, Y.; Xinyu, Z. Retrieval of land surface temperature from FY3D MERSI-II based on re-fitting Split Window Algorithm. *Eur. J. Remote Sens.* **2022**, *55*, 1–18. [CrossRef]
47. Abbasi, B.; Qin, Z.; Du, W.; Fan, J.; Li, S.; Zhao, C. Spatiotemporal Variation of Land Surface Temperature Retrieved from FY-3D MERSI-II Data in Pakistan. *Appl. Sci.* **2022**, *12*, 10458. [CrossRef]
48. Chen, H.; Meng, X.; Li, L.; Ni, K. Quality Assessment of FY-3D/MERSI-II Thermal Infrared Brightness Temperature Data from the Arctic Region: Application to Ice Surface Temperature Inversion. *Remote Sens.* **2022**, *14*, 6392. [CrossRef]
49. Chen, J.; Yao, Q.; Chen, Z.; Li, M.; Hao, Z.; Liu, C.; Zheng, W.; Xu, M.; Chen, X.; Yang, J.; et al. The Fengyun-3D (FY-3D) global active fire product: Principle, methodology and validation. *Earth Syst. Sci. Data* **2022**, *14*, 3489–3508. [CrossRef]
50. Zheng, W.; Chen, J.; Tang, S.-H.; Hu, X.-Q.; Liu, C. Fire monitoring based on FY-3D/MERSI-II far-infrared data. *J. Infrared Millim. Waves* **2020**, *39*, 120–127.
51. Zheng, W.; Chen, J.; Yan, H.; Liu, C.; Tang, S.H. Global fire monitoring products of FY-3D/MERSI-II and their applications. *J. Remote Sens.* **2020**, *24*, 521–530.
52. Dong, Z.; Yu, J.; An, S.; Zhang, J.; Li, J.; Xu, D. Forest Fire Detection of FY-3D Using Genetic Algorithm and Brightness Temperature Change. *Forests* **2022**, *13*, 963. [CrossRef]

53. Li, J.; Ge, S.; Gao, H. FY-3D MERSI Data for Active Fire Detection Based on Improved Multi-Temporal Algorithm. In Proceedings of the IGARSS 2022—IEEE International Geoscience and Remote Sensing Symposium, Kuala Lumpur, Malaysia, 17–22 July 2022; pp. 3528–3531. [CrossRef]
54. Ganci, G.; Cappello, A.; Neri, M. Data Fusion for Satellite-Derived Earth Surface: The 2021 Topographic Map of Etna Volcano. *Remote Sens.* **2023**, *15*, 198. [CrossRef]
55. Bonaccorso, A.; Bonforte, A.; Calvari, S.; Del Negro, C.; Di Grazia, G.; Ganci, G.; Neri, M.; Vicari, A.; Boschi, E. The initial phases of the 2008–2009 Mount Etna eruption: A multidisciplinary approach for hazard assessment. *J. Geophys. Res.* **2011**, *116*, B03203. [CrossRef]
56. Andronico, D.; Cannata, A.; Di Grazia, G.; Ferrari, F. The 1986–2021 paroxysmal episodes at the summit craters of Mt. Etna: Insights into volcano dynamics and hazard. *Earth-Sci. Rev.* **2021**, *220*, 103686. [CrossRef]
57. Bisson, M.; Spinetti, C.; Andronico, D.; Palaseanu-Lovejoy, M.; Buongiorno, M.F.; Alexandrov, O.; Cecere, T. Ten years of volcanic activity at Mt Etna: High-resolution mapping and accurate quantification of the morphological changes by Pleiades and Lidar data. *Int. J. Appl. Earth Obs. Geoinf.* **2021**, *102*, 102369. [CrossRef]
58. Viccaro, M.F.; Zuccarello, A.; Cannata, P.M.; Gresta, S. How a complex basaltic volcanic system works: Constraints from integrating seismic, geodetic, and petrological data at Mount Etna volcano during the July–August 2014 eruption. *J. Geophys. Res. Solid Earth* **2016**, *121*, 5659–5678. [CrossRef]
59. Ganci, G.; Bilotta, G.; Zuccarello, F.; Calvari, S.; Cappello, A. A Multi-Sensor Satellite Approach to Characterize the Volcanic Deposits Emitted during Etna's Lava Fountaining: The 2020–2022 Study Case. *Remote Sens.* **2023**, *15*, 916. [CrossRef]
60. Del Negro, C.; Cappello, A.; Neri, M.; Bilotta, G.; Hérault, A.; Ganci, G. Lava flow hazards at Mount Etna: Constraints imposed by eruptive history and numerical simulations. *Sci. Rep.* **2013**, *3*, 3493. [CrossRef] [PubMed]
61. Ferlito, C.; Coltorti, M.; Lanzafame, G.; Giacomoni, P.P. The volatile flushing triggers eruptions at open conduit volcanoes: Evidence from Mount Etna volcano (Italy). *Lithos* **2014**, *184*, 447–455. [CrossRef]
62. Moretti, R.; Métrich, N.; Arienzo, I.; Di Renzo, V.; Aiuppa, A.; Allard, P. Degassing vs. eruptive styles at Mt. Etna volcano (Sicily, Italy). Part I: Volatile stocking, gas fluxing, and the shift from low-energy to highly explosive basaltic eruptions. *Chem. Geol.* **2018**, *482*, 1–17. [CrossRef]
63. Calvari, S.; Nunnari, G. Comparison between Automated and Manual Detection of Lava Fountains from Fixed Monitoring Thermal Cameras at Etna Volcano, Italy. *Remote Sens.* **2022**, *14*, 2392. [CrossRef]
64. Palaseanu-Lovejoy, M.; Bisson, M.; Spinetti, C.; Buongiorno, M.F.; Alexandrov, O.; Cecere, T. High-Resolution and Accurate Topography Reconstruction of Mount Etna from Pleiades Satellite Data. *Remote Sens.* **2019**, *11*, 2983. [CrossRef]
65. Borzi, A.M.; Giuffrida, M.; Zuccarello, F.; Palano, M.; Viccaro, M. The Christmas 2018 eruption at Mount Etna: Enlightening how the volcano factory works through a multiparametric inspection. *Geochem. Geophys. Geosyst.* **2020**, *21*, e2020GC009226. [CrossRef]
66. Aloisi, M.; Jin, S.; Pulvirenti, F.; Scaltrito, A. The December 2015 Mount Etna eruption: An analysis of inflation/deflation phases and faulting processes. *J. Geodyn.* **2017**, *107*, 34–45. [CrossRef]
67. Bonaccorso, A.; Calvari, S. A new approach to investigate an eruptive paroxysmal sequence using camera and strainmeter networks: Lessons from the 3–5 December 2015 activity at Etna volcano. *Earth Planet. Sci. Lett.* **2017**, *475*, 231–241. [CrossRef]
68. Cannata, A.; Di Grazia, G.; Giuffrida, M.; Gresta, S.; Palano, M.; Sciotto, M.; Viccaro, M.; Zuccarello, F. Space-time evolution of magma storage and transfer at Mt. Etna volcano (Italy): The 2015–2016 reawakening of Voragine crater. *Geochem. Geophys. Geosyst.* **2018**, *19*, 471–495. [CrossRef]
69. Corsaro, R.A.; Andronico, D.; Behncke, B.; Branca, S.; Caltabiano, T.; Ciancitto, F.; Cristaldi, A.; de Beni, E.; la Spina, A.; Lodato, L.; et al. Monitoring the December 2015 summit eruptions at Mt. Etna (Italy): Implications on eruptive dynamics. *J. Volcanol. Geotherm. Res.* **2017**, *341*, 53–69. [CrossRef]
70. Laiolo, M.; Ripepe, M.; Cigolini, C.; Coppola, D.; Della Schiava, M.; Genco, R.; Innocenti, L.; Lacanna, G.; Marchetti, E.; Massimetti, F.; et al. Space-and Ground-Based Geophysical Data Tracking of Magma Migration in Shallow Feeding System of Mount Etna Volcano. *Remote Sens.* **2019**, *11*, 1182. [CrossRef]
71. Calvari, S.; Nunnari, G. Etna Output Rate during the Last Decade (2011–2022): Insights for Hazard Assessment. *Remote Sens.* **2022**, *14*, 6183. [CrossRef]
72. Guerrieri, L.; Corradini, S.; Theys, N.; Stelitano, D.; Merucci, L. Volcanic Clouds Characterization of the 2020–2022 Sequence of Mt. Etna Lava Fountains Using MSG-SEVIRI and Products' Cross-Comparison. *Remote Sens.* **2023**, *15*, 2055. [CrossRef]
73. Global Volcanism Program. *Report on Etna (Italy) In Bulletin of the Global Volcanism Network*; Bennis, K.L., Venzke, E., Eds.; Smithsonian Institution: Washington, DC, USA, 2022; Volume 47. [CrossRef]
74. INGV. Bollettino Mensile—Mese di Riferimento Novembre 2022. Issued 06/12/2022. Rep. N. M11/2022 ETNA. In Italian. 2022. Available online: https://www.ct.ingv.it/index.php/monitoraggio-e-sorveglianza/prodotti-del-monitoraggio/bollettini-settimanali-multidisciplinari/716-bollettino-Mensile-sul-monitoraggio-vulcanico-geochimico-e-sismico-del-vulcano-Etna-del-2022-12-06/file (accessed on 5 February 2022).
75. INGV. Bollettino Settimanale—Settimana di Riferimento 06/02/2023-12/02/2023. Issued 14/02/2023. Rep. N. 07/2023 ETNA. In Italian. 2023. Available online: https://www.ct.ingv.it/index.php/monitoraggio-e-sorveglianza/prodotti-del-monitoraggio/bollettini-settimanali-multidisciplinari/744-bollettino-Settimanale-sul-monitoraggio-vulcanico-geochimico-e-sismico-del-vulcano-Etna-del-2023-02-14/file (accessed on 3 March 2022).

76. Chen, Z.; Xie, J.; Heygster, G.; Chi, Z.; Yang, L.; Wu, S.; Hui, F.; Cheng, X. A Simplified Coastline Inflection Method for Correcting Geolocation Errors in FengYun-3D Microwave Radiation Imager Images. *Remote Sens.* **2023**, *15*, 813. [CrossRef]
77. Zhang, P. Fengyun Meteorological Satellites and Consideration on Calibration Issues. In *Proceedings of the 99th American Meteorological Society Annual Meeting*; Phoenix, AZ, USA, 6–10 January 2019, AMS: Phoenix, AZ, USA, 2019.
78. Jing, Z.; Li, S.; Hu, X.; Tang, F. Sub-pixel accuracy evaluation of FY-3D MERSI-2 geolocation based on OLI reference imagery. *Int. J. Remote Sens.* **2021**, *42*, 7215–7238. [CrossRef]
79. Pan, H.; Cui, Z.; Hu, X.; Zhu, X. Systematic Geolocation Errors of FengYun-3D MERSI-II. In *IEEE Transactions on Geoscience and Remote Sensing*; IEEE: Piscataway, NJ, USA, 2022; Volume 60, pp. 1–11. [CrossRef]
80. Tang, K.H.; Zhu, P.; Ni, L.R.; Fan, C. Retrieving Land Surface Temperature From Chinese FY-3D MERSI-2 Data Using an Operational Split Window Algorithm. *IEEE J. Sel. Top. Appl. Earth Obs. Remote Sens.* **2021**, *14*, 6639–6651. [CrossRef]
81. Na, X.; Wu, R.; Hu, X. *Guidelines for the Use of Medium-Resolution Spectral Imager Data in the D-Satellite Medium-Resolution Spectral Imager of Fengyun-3 (Batch 02) Meteorological Satellite Ground Application System Engineering. National Satellite Meteorological Center. L1 Data Product*; Version 2.1, July 2019; Data Usage Guidelines; China Meteorological Administration: Beijing, China, 2019. (In Chinese)
82. Liu, L.; Wen, X.; Dong, X.; Dai, Q. A New Prompt Algorithm for Removing Bowtie Effect of MODIS L1B Data. In Proceedings of the 2008 Congress on Image and Signal Processing, Sanya, China, 27–31 May 2008; pp. 663–667. [CrossRef]
83. Nishihama, M.; Wolfe, R.; Solomon, D.; Patt, F.; Blanchette, J.; Fleig, A.; Masuoka, E. *MODIS level 1A Earth Location: Algorithm Theoretical Basis Document*, version 3.0. SDST-092; MODIS Science Data Support Team: Sioux Falls, SD, USA, 1997.
84. Global Volcanism Program. *(Database) Volcanoes of the World*; v. 5.0.2; 23 January 2023; Smithsonian Institution: Washington, DC, USA, compiled by Venzke, E.; 2023. [CrossRef]
85. Wooster, M.J.; Zhukov, B.; Oertel, D. Fire radiative energy for quantitative study of biomass burning: Derivation from the BIRD experimental satellite and comparison to MODIS fire products. *Remote Sens. Environ.* **2003**, *86*, 83–107. [CrossRef]
86. Wang, M.; He, G.; Zhang, Z.; Wang, G.; Wang, Z.; Yin, R.; Cui, S.; Wu, Z.; Cao, X. A Radiance-Based Split-Window Algorithm for Land Surface Temperature Retrieval: Theory and Application to MODIS Data. *Int. J. Appl. Earth Obs. Geoinf.* **2019**, *76*, 204–217. [CrossRef]
87. Coppola, D.; Barsotti, S.; Cigolini, C.; Laiolo, M.; Pfeffer, M.A.; Ripepe, M. Monitoring the time-averaged discharge rates, volumes and emplacement style of large lava flows by using MIROVA system: The case of the 2014-2015 eruption at Holuhraun (Iceland). *Ann. Geophys.* **2019**, *61*, VO221. [CrossRef]
88. Coppola, D.; Laiolo, M.; Piscopo, D.; Cigolini, C. Rheological control on the radiant density of active lava flows and domes. *J. Volcanol. Geotherm. Res.* **2013**, *249*, 39–48. [CrossRef]
89. Cao, C.; Xiong, X.; Wolfe, R.; DeLuccia, F.; Liu, Q.; Blonski, S.; Lin, G.; Nishihama, M.; Pogorzala, D.; Oudrari, H.; et al. *Visible Infrared Imaging Radiometer Suite (VIIRS) Sensor Data Record (SDR) User's Guide*; Version 1.3, NOAA Technical Report NESDIS; NESDIS: College Park, MD, USA, 2017.
90. Marchese, F.; Filizzola, C.; Lacava, T.; Falconieri, A.; Faruolo, M.; Genzano, N.; Mazzeo, G.; Pietrapertosa, C.; Pergola, N.; Tramutoli, V.; et al. Mt. Etna Paroxysms of February–April 2021 Monitored and Quantified through a Multi-Platform Satellite Observing System. *Remote Sens.* **2021**, *13*, 3074. [CrossRef]
91. D'Aleo, R.; Bitetto, M.; Delle Donne, D.; Coltelli, M.; Coppola, D.; McCormick Kilbride, B.; Pecora, E.; Ripepe, M.; Salem, L.C.; Tamburello, G.; et al. Understanding the SO2 Degassing Budget of Mt Etna's Paroxysms: First Clues From the December 2015 Sequence. *Front. Earth Sci.* **2019**, *6*, 239. [CrossRef]
92. Coppola, D.; James, M.R.; Staudacher, T.; Cigolini, C. A comparison of field-and satellite-derived thermal flux at Piton de la Fournaise: Implications for the calculation of lava discharge rate. *Bull. Volcanol.* **2010**, *72*, 341–356. [CrossRef]
93. Lipman, P.W.; Banks, N.G. AA flow dynamics, Mauna Loa 1984. In *US Geol Surv Prof Pap*; HVO: Washington, DC, USA, 1987; Volume 1350, pp. 1527–1567.
94. China Aerospace Science and Technology Corporation (CASC) 'China Launches New Remote Sensing Satellite'. Haidian District, Beijing 100048, PRC, 2023-02-24 (Online). Available online: http://english.spacechina.com/n16421/n17212/c3743905/content.html (accessed on 1 March 2023).
95. Xie, L.; Wu, S.; Chen, J.; Zheng, W.; Yan, H.; Xu, Z. Cross-Comparison of channel parameters between FY-3E/MERSI-LL and Himawari-8/AHI in China. *Int. J. Remote Sensing* **2022**, *43*, 4663–4681. [CrossRef]
96. Lowenstern, J.B.; Ewert, J.W.; Lockhart, A.B. Strengthening local volcano observatories through global collaborations. *Bull. Volcanol.* **2022**, *84*, 10. [CrossRef]